



# Spray-dried ternary bioactive glass microspheres: Direct and indirect structural effects of copper-doping on acellular degradation behavior

Gabriele Vecchio, Vincent Darcos, Sylvain Le Grill, Fabien Brouillet, Yannick Coppel, Mathieu Duttine, Alessandro Pugliara, Christèle Combes, Jérémy Soulié

## ► To cite this version:

Gabriele Vecchio, Vincent Darcos, Sylvain Le Grill, Fabien Brouillet, Yannick Coppel, et al.. Spray-dried ternary bioactive glass microspheres: Direct and indirect structural effects of copper-doping on acellular degradation behavior. *Acta Biomaterialia*, 2024, 181, pp.453-468. 10.1016/j.actbio.2024.05.003 . hal-04607086

**HAL Id: hal-04607086**

**<https://hal.science/hal-04607086v1>**

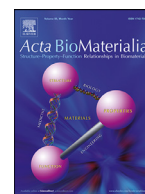
Submitted on 10 Jun 2024

**HAL** is a multi-disciplinary open access archive for the deposit and dissemination of scientific research documents, whether they are published or not. The documents may come from teaching and research institutions in France or abroad, or from public or private research centers.

L'archive ouverte pluridisciplinaire **HAL**, est destinée au dépôt et à la diffusion de documents scientifiques de niveau recherche, publiés ou non, émanant des établissements d'enseignement et de recherche français ou étrangers, des laboratoires publics ou privés.



Distributed under a Creative Commons Attribution - NoDerivatives 4.0 International License



## Full length article

# Spray-dried ternary bioactive glass microspheres: Direct and indirect structural effects of copper-doping on acellular degradation behavior



Gabriele Vecchio<sup>a,b</sup>, Vincent Darcos<sup>a</sup>, Sylvain Le Grill<sup>b</sup>, Fabien Brouillet<sup>b</sup>, Yannick Coppel<sup>c</sup>, Mathieu Duttine<sup>d</sup>, Alessandro Pugliara<sup>b,e</sup>, Christèle Combes<sup>b</sup>, Jérémy Soulié<sup>b,\*</sup>

<sup>a</sup> Institut des Biomolécules Max Mousseron (IBMM), University of Montpellier, CNRS, ENSCM, 34293 Montpellier, France

<sup>b</sup> CIRIMAT, Toulouse INP, Université Toulouse 3 Paul Sabatier, CNRS, Université de Toulouse, ENSIACET, 31030 Toulouse, France

<sup>c</sup> Laboratoire de Chimie de Coordination (LCC), Université de Toulouse, CNRS, UPR 8241, Université Toulouse 3 – Paul Sabatier, Toulouse 31077, France

<sup>d</sup> Université de Bordeaux, CNRS, Bordeaux INP, ICMCB, UMR 5026, Pessac F-33600, France

<sup>e</sup> Centre de MicroCaractérisation Raimond Castaing, Université Toulouse 3 – Paul Sabatier, Toulouse INP, INSA Toulouse, CNRS, 31400 Toulouse, France

## ARTICLE INFO

## Article history:

Received 28 February 2024

Revised 16 April 2024

Accepted 1 May 2024

Available online 7 May 2024

## Keywords:

Bioactive glasses

Spray-drying

Copper

Microspheres

## ABSTRACT

Silicate-based bioactive glass nano/microspheres hold significant promise for bone substitution by facilitating osteointegration through the release of biologically active ions and the formation of a biomimetic apatite layer. Cu-doping enhances properties such as pro-angiogenic and antibacterial behavior. While sol-gel methods usually yield homogeneous spherical particles for pure silica or binary glasses, synthesizing poorly aggregated Cu-doped ternary glass nano/microparticles without a secondary CuO crystalline phase remains challenging. This article introduces an alternative method for fabricating Cu-doped ternary microparticles using sol-gel chemistry combined with spray-drying. The resulting microspheres exhibit well-defined, poorly aggregated particles with spherical shapes and diameters of a few microns. Copper primarily integrates into the microspheres as Cu<sup>0</sup> nanoparticles and as Cu<sup>2+</sup> within the amorphous network. This doping affects silica network connectivity, as calcium and phosphorus are preferentially distributed in the glass network (respectively as network modifiers and formers) or involved in amorphous calcium phosphate nano-domains depending on the doping rate. These differences affect the interaction with simulated body fluid. Network depolymerization, ion release (SiO<sub>4</sub><sup>4-</sup>, Ca<sup>2+</sup>, PO<sub>4</sub><sup>3-</sup>, Cu<sup>2+</sup>), and apatite nanocrystal layer formation are impacted, as well as copper release. The latter is mainly provided by the copper involved in the silica network and not from metal nanoparticles, most of which remain in the microspheres after interaction. This understanding holds promising implications for potential therapeutic applications, offering possibilities for both short-term and long-term delivery of a tunable copper dose.

## Statement of significance

A novel methodology, scalable to industrial levels, enables the synthesis of copper-doped ternary bioactive glass microparticles by combining spray-drying and sol-gel chemistry. It provides precise control over the copper percentage in microspheres. This study explores the influence of synthesis conditions on the copper environment, notably Cu<sup>0</sup> and Cu<sup>2+</sup> ratios, characterized by EPR spectroscopy, an aspect poorly described for copper-doped bioactive glass. Additionally, copper indirectly affects silica network connectivity and calcium/phosphorus distribution, as revealed by SSNMR. Multiscale characterization illustrates how these features impact acellular degradation in simulated body fluid, highlighting the therapeutic potential for customizable copper dosing to address short- and long-term needs.

© 2024 The Author(s). Published by Elsevier Ltd on behalf of Acta Materialia Inc.

This is an open access article under the CC BY-NC-ND license

(<http://creativecommons.org/licenses/by-nc-nd/4.0/>)

\* Corresponding author.

E-mail address: [jeremy.soulie@toulouse-inp.fr](mailto:jeremy.soulie@toulouse-inp.fr) (J. Soulié).

## 1. Introduction

In the field of maxillofacial surgery, small bone defects resulting from pathologies or previous surgical procedures require the use of medical implants for bone reconstruction. These implants, typically a few cubic centimetres in size, play a crucial role in stimulating new bone formation, promoting cell adhesion, and providing structural support. They should also exhibit properties such as high porosity to enhance cell colonization and angiogenesis, maintain mechanical stability during surgical manipulation, and resorb over time. Among the various inorganic materials, silicate-based bioactive glasses (BG), meet several of these criteria. In particular, they are capable of promoting the osteointegration when implanted in bone defects [1–3]. Indeed, they tend to degrade and release active ions ( $\text{SiO}_4^{4-}$ ,  $\text{Ca}^{2+}$ ,  $\text{PO}_4^{3-}$ ). The silicon and calcium are known to play a role in osteoblast proliferation, differentiation [4,5], and the expression of growth factors (IGF-I/II) and proteins (BMPs), which are crucial regulators of bone formation [6]. Additionally, calcium and phosphate ions are both involved in the formation of an interfacial biomimetic apatite layer [7] that enhances cells adhesion and proliferation [1].

Beyond these general considerations, the treatment of certain pathologies such as mandibular osteoradionecrosis requires additional properties and especially pro-angiogenic and antibacterial behaviour [8]. Among several approaches [9] to enhance therapeutic potential of implants, the addition of copper is a promising way both in its metallic form ( $\text{Cu}^0$ ) and when incorporated in the glassy matrix as doping ions ( $\text{Cu}^+$  and  $\text{Cu}^{2+}$ ) [10].  $\text{Cu}^{2+}$  ions in solution possess a high antibacterial activity against various bacterial strains, and Cu-doped biomaterials prevent a biofilm formation [9,11–14]. The most proposed killing mechanism is related to  $\text{Cu}^{2+}$  tendency to form highly reactive oxygen species (ROS) that damage the DNA or denature proteins and consequently lead to bacterial death [15–19]. Additionally, Cu ions can play a fundamental role in angiogenesis [15,20,21], this process being predominant since blood vessels are essentials for the delivery of (micro)nutrients to cells and hence for a proper development of the bone tissue [10,22,23]. Despite beneficial effects, high concentration of  $\text{Cu}^{2+}$  might result in serious toxic effects, neurodegenerative diseases, and cell death by oxidative stress [24–26].

As stated previously, in addition to the biological impact of constitutive ions, the shaping of implants plays a key role in their osseointegration. In particular, in order to mimic the structure of mandibular trabecular bone, biomaterials should possess an open macroporosity. The brittleness of bioactive glasses limits their use as bulk materials for cyclic load applications and surgical cutting. To overcome these limitations, composite materials combining bio-glasses with polymers have been developed. Several manufacturing processes, including electrospinning [27], 3D printing [28] or freeze-casting [8], have been explored to produce such porous composites. Previous methods of combining bioactive glasses with polymers have shown drawbacks like poor charge dispersion and spatial inhomogeneity of properties. This can lead to the degradation of certain regions and weakening of the pore walls. Decreasing the size of the glass particles has been shown to address this issue [8]. Sol-gel method allows to obtain homogeneous spherical particles with controllable size ranging from the nanoscale up to few microns [29]. Despite the feasibility of the technique, sol-gel synthesis of nanoparticles requires high amounts of inflammable solvents and results into low yields, thus making it unsuitable for industrial purposes [30,31]. Besides and to the best of our knowledge, the synthesis of dense nano/microparticles combining the following properties is still a challenge: i) quaternary glasses composed of Si, Ca, P and Cu oxides, ii) high and/or total integration rate of P and Cu without secondary stable crystalline phase such as CuO [32], iii) poorly aggregated nanoparticles highly dispersible.

The spray-drying process is an interesting alternative to “pure sol-gel” as it is a versatile technique especially designed for large industrial purposes [33,34]. In the last two decades spray-drying process gained a great importance for drug encapsulation [35], the synthesis of core-shell materials [36] or micron-sized nanoaggregates [37]. Silica-based and non-aggregated microparticles (MPs) can be obtained by spray-drying, starting from alkoxide precursors solutions [38–40]. Indeed, the solution is sprayed through a nozzle thanks to a stream of gas, producing a dispersion of micro-droplets in which the precursors are present in desired concentrations, thus acting like microreactors [41]. Due to the high temperature and the consequent rapid evaporation of the solvent, the droplet shrinks and the condensation reaction of silica precursor is triggered because of the increase in concentration and the confinement imposed by the droplet [38]. Finally, thanks to the applied vacuum, the dried particles are collected in the bottom of the cyclone collector [33]. Several operational parameters [34,39,42–44] or formulation parameters [45–47] could impact morphological and textural characteristics of MPs.

Most of the studies carried out on spray-dried MPs are referred to the synthesis of spherical silica MPs [40,44,48] and only a few works focus on the synthesis of bioactive glass MPs by spray-drying. Among them, Chou et al. [49] prepared ternary MPs with composition 58S, 68S, 76S and Ningsih et al. [50] synthesized Sr-doped quaternary MPs. Nevertheless, to the very best of our knowledge, we did not found studies reporting the introduction of copper or other transition metals in BG spray-dried particles. Moreover, despite the novelty of previous works the resulting particles are generally poorly characterized in particular from a structural point of view, whereas it is crucial to understand the further physico-chemical and biological behavior of such glasses.

Consequently, the present study aspires to demonstrate the feasibility of copper-doped ternary glass synthesis by spray-drying and to understand i) how copper doping rate could directly impact the oxidation state of copper, and its spatial distribution in spray-dried microspheres, ii) how it could affect the connectivity and homogeneity of the silica network and iii) how it impacts the degradation properties of such particles and their acellular *in vitro* behavior. With this aim, different samples with increasing Cu content were synthesized and their morphological and structural properties were thoroughly characterized in particular by transmission and scanning electron microscopies, laser granulometry, solid state nuclear magnetic resonance, electron paramagnetic resonance and X-ray diffraction. *In vitro* acellular reactivity and ion release profile of the BG MPs were evaluated by immersing the powders in simulated body fluids (SBF).

## 2. Experimental section

### 2.1. Precursors

Tetraethyl orthosilicate (TEOS, 99 %), triethyl phosphate (TEP, 99 %), calcium nitrate tetrahydrate ( $\text{Ca}(\text{NO}_3)_2 \cdot 4\text{H}_2\text{O}$ , CaNT) and hydrochloric acid (37 % v/v) were purchased from Merck. Copper (II) nitrate trihydrate ( $\text{Cu}(\text{NO}_3)_2 \cdot 3\text{H}_2\text{O}$ , 99 %, CuNT) and ethanol absolute were provided by VWR Chemicals. All the reactants involved in the preparation of simulated body fluid (SBF) solution, sodium chloride ( $\text{NaCl}$ ,  $\geq 98$  %), potassium chloride (KCl, 99.5–101.0 %), magnesium chloride hexahydrate ( $\text{MgCl}_2 \cdot 6\text{H}_2\text{O}$ , 99.0–101.1 %), calcium chloride dihydrate ( $\text{CaCl}_2 \cdot 2\text{H}_2\text{O}$ , 99.0–103.0 %), di-potassium hydrogen phosphate trihydrate ( $\text{K}_2\text{HPO}_4 \cdot 3\text{H}_2\text{O}$ ,  $\geq 99$  %), sodium sulphate anhydrous ( $\text{Na}_2\text{SO}_4$ , 98.5–101.0 %), tris-(hydroxymethyl) aminomethane (TRIS,  $\geq 99$  %) and sodium hydrogen carbonate ( $\text{NaHCO}_3$ , 100.1 %) were of analytical grade and provided by VWR chemicals. All the chemicals were used as received, without

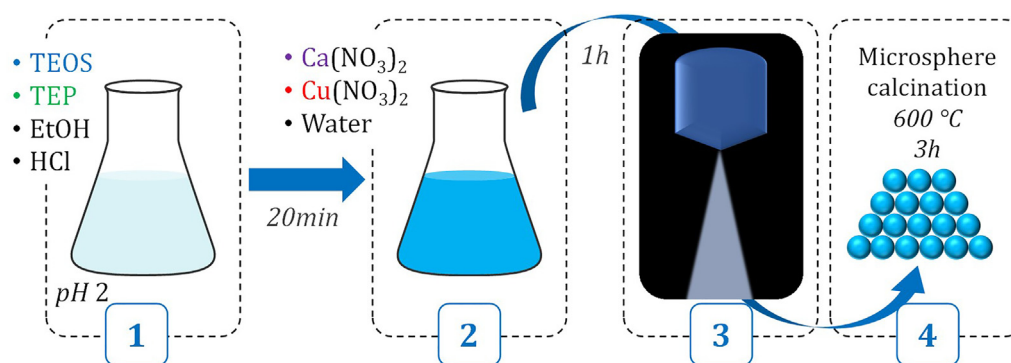


**Fig. 1.** Principle scheme of synthesis by spray-drying of Cu-doped bioactive glass microspheres: (1) hydrolysis of silicon and phosphorus alkoxides, (2) addition of calcium and copper nitrate precursors, (3) spray-drying, (4) powder calcination.

further purification. Ultrapure water ( $\rho = 18.2 \text{ M}\Omega\cdot\text{cm}$ ) was obtained through Millipore Milli-Q water system.

## 2.2. Synthesis Cu-doped bioactive glass microspheres coupling sol-gel and spray-drying

Cu-doped BG microspheres with composition  $\text{SiO}_2\text{-CaO-P}_2\text{O}_5\text{-CuO}$  were synthesized by coupling the sol-gel method and the spray-drying process (Fig. 1). Four compositions of MPs, each with varying Cu content, were obtained by substituting copper for the Ca cations. The nominal compositions were  $67.5\text{SiO}_2$ ,  $(25-x)\text{CaO}$ ,  $7.5\text{P}_2\text{O}_5$ ,  $(x)\text{CuO}$  (at.%), where  $x = 0, 1, 2.5, 5$  at.%.

First, the solution containing the precursors was prepared under acidic conditions ( $\text{pH} = 2$ ). The acidic environment was chosen in order to favour the hydrolysis reaction of the network formers over their condensation. HCl 0.5 M and absolute ethanol were poured into an Erlenmeyer flask, stirred at 750 rpm with a magnetic bar and covered with Parafilm to prevent solvents evaporation. After 15 min, TEP was added to the solution, and 30 min later TEOS was added rapidly. The solution was stirred for further 20 min, then the CaNT and CuNT, previously dissolved in half of the ultrapure water needed for the synthesis, were added and the mixture was left to stir until a clear and homogeneous solution was obtained. Then, the rest of the water was added rapidly. The volume ratios of ethanol, HCl and water were fixed with respect to the TEOS as follows:  $\text{TEOS}/\text{EtOH} = 0.82$ ,  $\text{TEOS}/\text{HCl} = 38.47$ ,  $\text{TEOS}/\text{water} = 0.37$ . Ternary MPs solution ( $x = 0$  at.%) was prepared in the same way, but without employing the copper nitrate precursor.

Once the solution was clear again, it was atomized through a Mini Spray Dryer B 290 (BÜCHI, Switzerland). The inlet/outlet temperatures ( $T_{\text{in}}/T_{\text{out}}$ ) were set at  $180/100^\circ\text{C}$ , the air flow at  $1052 \text{ L}\cdot\text{h}^{-1}$ , the solution feed rate at  $3 \text{ mL}\cdot\text{min}^{-1}$  (pump = 10 %), and the applied vacuum at approximately 50 mbar (aspirator 90 %).

The obtained powders were dried in a ventilated oven at  $50^\circ\text{C}$  overnight, and then they underwent a thermal treatment at  $600^\circ\text{C}$  for 2 h with a heating rate of  $5^\circ\text{C}\cdot\text{min}^{-1}$ .

The resulting powders were labelled as 0-BG MPs, 1-BG MPs, 2.5-BG MPs, 5-BG MPs, where the number on the left corresponds to the atomic% of substituting copper. With this method we were able to obtain up to 6.8 g of raw MPs (yield ~ 62 %) with a single sprayed batch (130 mL), since it was estimated that the required spray-drying time (45 min) was short enough to prevent the formation of nanoparticles that could obstruct the spray nozzle.

## 2.3. Characterization

Particles size distribution was determined for 1 g of powder by laser granulometry using a Mastersizer 3000 (Malvern instru-

ments, UK) with an Aero S module ( $p = 3$  bars, 10% obturation, 30 s accumulation). Specific surface area (SSA) for 0.5 g of MPs was estimated by  $\text{N}_2$  adsorption/desorption through the Brunauer-Emmet-Teller method (BET) on a Monosorb Quantachrom MS-22 instrument. Samples were outgassed at  $120^\circ\text{C}$  overnight prior to analysis.

The surface electrical charge of the MPs was determined by Z-potential ( $\zeta$ ) measurements on a Zetasizer Pro (Malvern instruments, UK). Samples were previously dispersed by ultrasounds (18 W ultrasound microtip) for 5 min in deionized water with a concentration of  $1 \text{ mg}\cdot\text{mL}^{-1}$ . Fourier-transform infrared spectroscopy (FT-IR) was carried out with a Nicolet iS50 spectrophotometer (Thermo Scientific, USA), in transmission mode, in a range of  $400\text{--}4000 \text{ cm}^{-1}$  with a resolution of  $2 \text{ cm}^{-1}$  and 64 cumulative scans. Samples were compressed into KBr pellets ( $\sim 1 \text{ mg}$  of sample per 300 mg of KBr) before the analysis.

X-ray diffraction (XRD) was performed using a Bruker D8-2 ADVANCE X-ray diffractometer for powders (Bruker, Germany), using a  $\text{Cu K}\alpha$  X-ray source ( $\lambda_{\text{Cu K}\alpha} = 1.54056 \text{ \AA}$ ) and carrying out the analysis in a  $2\theta$  range of  $10^\circ\text{--}90^\circ$ . A step size of  $0.01^\circ$  with a dwell time of 1 s per step was employed. Powders were placed on low-background PMMA sample holders prior to analysis.

Particle's morphology was observed by scanning electron microscopy (SEM) with a FEI Quanta450 in low vacuum mode (water vapor pressure: 90 Pa). Images were registered in secondary electron mode (SE), with a working distance around 10 mm and an accelerating voltage of 12.5 kV. Samples were sputtered with silver plasma for 3 min prior to be examined, using a Scancoat 6 Sputter Coater. SEM-Energy-dispersive X-ray spectroscopy (EDX) was also carried out in order to determine the particles elemental composition. Samples were compressed into pellets and fixed on the SEM supports by means of a carbon adhesive strip.

To prepare samples for Transmission electron microscopy (TEM) observations and analysis, MPs were dispersed in epoxy resin for 48 h at  $60^\circ\text{C}$ . The resin was then dry cut (50 nm thickness) with an ultramicrotome (Leica UC7) and picked up onto a nickel grid. TEM images of the MPs' sections were taken with a JEOL JEM-1400 transmission electron microscope (Japan) with an acceleration of 120 kV and equipped with a Orius 1000 Gatan (USA) camera. Moreover, Scanning TEM (STEM) - High-angle annular dark-field (HAADF) images and STEM-EDX mapping of 5-BG MPs sample for the main elements composing the particles (Si, P, Ca, Cu) were performed on a transmission electron microscope JEOL JEM-2100F operating at an accelerated voltage of 200 kV equipped with EDX analyzer Oxford instrument UltimMax 100  $\text{mm}^2$  (UK) and equipped with a STEM module Digiscan III of Gatan.

Electron Paramagnetic Resonance (EPR) powder spectra were recorded at room temperature with a Bruker ESP-300E X-band spectrometer equipped with a rectangular TE104 resonant cavity.



The main spectroscopic parameters were microwave with 9.54 GHz frequency and 20 mW power, magnetic field modulation with 100 kHz frequency and 0.5 mT amplitude, 0.3 mT/pt spectral resolution and 82 ms conversion time. DPPH EPR signal ( $g = 2.0036$ ) was used as external reference. Analyses of EPR data and signal simulation were performed with Bruker WinEPR and WinSIMFONIA software, respectively. The  $\text{Cu}^{2+}$  concentrations in the analyzed samples were estimated regarding to EPR spectra recorded for mixed powders of copper (II) sulphate pentahydrate and boron nitride with known copper content (ranging from  $1.2 \times 10^{-6}$  to  $1.5 \times 10^{-4}$  mol).

NMR experiments were recorded on a Bruker Avance 400 III HD spectrometer operating at magnetic fields of 9.4 T. Samples were packed into 4 mm rotors and were rotated at frequencies between 8 and 12 kHz at 295 K.  $^1\text{H}$  MAS were performed with the DEPTH pulse sequence and a recycle delay of 3 s.  $^{29}\text{Si}$  and  $^{31}\text{P}$  MAS NMR with direct polarization (DP) were performed with  $45^\circ$  pulses and recycle delays of 100 s and 300 s, respectively.  $^{29}\text{Si}$  and  $^{31}\text{P}$  CP MAS spectra were recorded with a recycle delay of 2 s and contact times of 2 ms and 5 ms, respectively. Chemical shifts were referenced to TMS and 85 %  $\text{H}_3\text{PO}_4$  for  $^1\text{H}$ ,  $^{29}\text{Si}$  and  $^{31}\text{P}$ , respectively.

## 2.4. Acellular in vitro evolution in simulated body fluid (SBF) solution

### 2.4.1. Bioactive glass/SBF interaction

The *in vitro* acellular bioactivity assessment of the synthesized Cu-BG MPs, were carried out in simulated body fluid (SBF) according to the method described by Kokubo and Takadama [51]. Firstly, a cationic ( $\text{NaCl}$ ,  $\text{KCl}$ ,  $\text{MgCl}_2 \cdot 6\text{H}_2\text{O}$ ,  $\text{CaCl}_2 \cdot 2\text{H}_2\text{O}$  and  $\text{HCl}$  1 M dissolved in ultrapure water) and an anionic ( $\text{NaCl}$ ,  $\text{K}_2\text{HPO}_4 \cdot 3\text{H}_2\text{O}$ ,  $\text{Na}_2\text{SO}_4$  and  $\text{HCl}$  1 M dissolved in ultrapure water) solutions with their respective pH adjusted to 7.4 by adding tris-(hydroxymethyl) aminomethane were mixed, and sodium hydrogen carbonate was added to the obtained SBF solution. Then, the powders were soaked in SBF with a concentration of  $3 \text{ mg} \cdot \text{mL}^{-1}$  and incubated at  $37^\circ\text{C}$  under continuous magnetic stirring (400 rpm). The time points evaluated were 1, 3, 6, 24 h, 7 and 14 days. At the end of each predetermined time, the suspensions were removed from the incubator, and the powders were separated from the SBF solutions by vacuum filtration, using cellulose ester membranes (Cytiva,  $D = 47 \text{ mm}$ , pore  $\phi = 0.22 \mu\text{m}$ , Whatman<sup>TM</sup>). The SBF solution was recovered, filtered again (CA syringe filter Avantor,  $D = 25 \text{ mm}$ , pore  $\phi = 0.22 \mu\text{m}$ , VWR) and stocked at  $4^\circ\text{C}$ , while the resulting powders were washed gently with ultrapure water, and then dried for 48 h at  $60^\circ\text{C}$  in a ventilated oven.

All the powders from the four Cu-BG MPs samples tested were characterized at different time points by FT-IR, SEM and XRD. More specifically, FT-IR spectra and XRD diffractograms were recorded for all the six time points, while SEM images only for 24 h, 7 and 14 days. EDX,  $^{29}\text{Si}$ ,  $^{31}\text{P}$  and  $^1\text{H}$  solid state NMR analysis were performed on 14 days samples. Conditions and procedures to characterize these samples are the same as described above.

### 2.4.2. Ion release profiles and pH changes

The ion release profile of the particles immersed in SBF was evaluated from the filtered SBF solutions collected at each time point by inductively coupled plasma optical emission spectroscopy (ICP-OES). Typically, solutions were diluted with demineralized water by a factor of 10, and analyzed with an Agilent 5800 VDV ICP-OES in radial mode. The standard ranges were calibrated using single-element solutions. Diluted SBF was also analyzed in order to obtain background values. The measurements were realized for all the sample solutions at each time point. Si, P, Ca and Cu concentrations were determined. The pH of every recovered sample solution was measured with a pHmeter inoLab pH7110 (3 points-calibrated with standards at pH 4.01, 7.000, 10.001).

## 2.5. Statistical analysis

Laser granulometry measurement was repeated three times for each sample, and the presented gaussian distributions are the result of their average.

Z-potential measurements were repeated three times for each sample and the results are reported as average values along with their standard deviations.

The molar composition determined by SEM-EDX was estimated over a  $100 \mu\text{m}^2$  square of the sample through the P/B ZAF method, and the values were averaged over four measurements.

Considering SBF tests, a triplicate powder suspension sample was prepared for each time point and for each Cu-BG MPs synthesized, for SBF tests. The powders of the triplicate sample for each time point were finally joined together, in order to have enough amount of each sample to be characterized.

The ICP-OES analysis were realized for all the sample solutions at each time point in duplicate. Si, P, Ca and Cu concentrations were determined and the data points were presented as averaged values  $\pm$  standard deviation for  $n = 2$ . The pH were measured in triplicate and results presented as averaged values  $\pm$  standard deviation for  $n = 3$ .

## 3. Results and discussion

### 3.1. As-synthesized Cu-doped microspheres

Four kinds of MPs were synthesized combining the sol-gel route with the spray-drying process. These microparticles of either ternary or quaternary glasses differ on their nominal composition, and more precisely on the amount of  $\text{Cu}^{2+}$ , from 0 to 5 at%. Each composition is described in Table 1.

Focusing first on morphological aspects, SEM images of 5-BG MPs are presented on Fig. 2-a and b as representative microspheres whatever the doping amount (SEM pictures of all samples are given in S1-a). They show well-defined and individual particles having a spherical shape. These microparticles exhibit diameters ranging from the submicrometric order up to a few microns. Compared to “pure” Stöber-derived methods [52,53], the rather broad size distribution is intrinsically related to the spray-drying technique. For all the samples the particles surface is quite rough, due to localized inhomogeneous evaporation of the droplet's solvent [45,54–56]. To implement this direct observation, the MPs size distributions were determined by laser granulometry (Figure S2), while the particles size percentile values  $D_{10}$ ,  $D_{90}$  and span are reported in Table S1. All the four samples exhibit a volume median diameter ( $D_{50}$ ) around  $3 \mu\text{m}$  (Table 1 and S1) with a bimodal particle size distribution (Figure S2). The main population corresponding to single particles can be observed in the range 1–10  $\mu\text{m}$ , while another small population can be distinguished in the range 10–100  $\mu\text{m}$ . This second population stems from large aggregates of particles (also observed with SEM), probably because the jet of compressed air of the particle size analyzer (3 bar) could not break some agglomerates. Considering  $D_{90}$  and span values, it can be assumed that 5 %-doped particles form larger aggregates than less Cu-doped particles. Nevertheless, and as expected for dense spray-dried silica-based microspheres [49], the  $\text{SSA}_{\text{BET}}$  are comprised between 3 and  $4 \text{ m}^2 \cdot \text{g}^{-1}$  and demonstrated the absence of intrinsic open porosity [57].

The actual composition of the synthesized bioglasses was determined by SEM-EDX and the results are shown in Table 1. SEM-EDX analysis confirmed that Cu was effectively integrated, and its content is very close to the nominal one, as well as the Si content. However, for all the samples the phosphorus content is at least half of the nominal value, fixed at 7.5 at% while the content of calcium is consequently higher. Low phosphorus content could be due to

**Table 1**  
Median diameters (laser granulometry), nominal and experimental composition by SEM-EDX and Cu<sup>0</sup> mean crystallites length of the spray-dried microspheres.

Sample	Particles size percentile value <i>D</i> <sub>50</sub> (μm)	Composition SiO <sub>2</sub> -CaO-P <sub>2</sub> O <sub>5</sub> -CuO		Cu <sup>0</sup> (111) crystallite size (nm)
		Nominal (at.%)	EDX (at.%)	
0-BG MPs	2.69	67.5/25/7.5/0	65/32/3/0	0
1-BG MPs	3.23	67.5/24/7.5/1	67.9/27.6/3.4/1.1	62
2.5-BG MPs	3.08	67.5/22.5/7.5/2.5	65/27.9/3.8/3.3	70
5-BG MPs	3.30	67.5/20/7.5/5	68.9/21.7/3.6/5.8	64

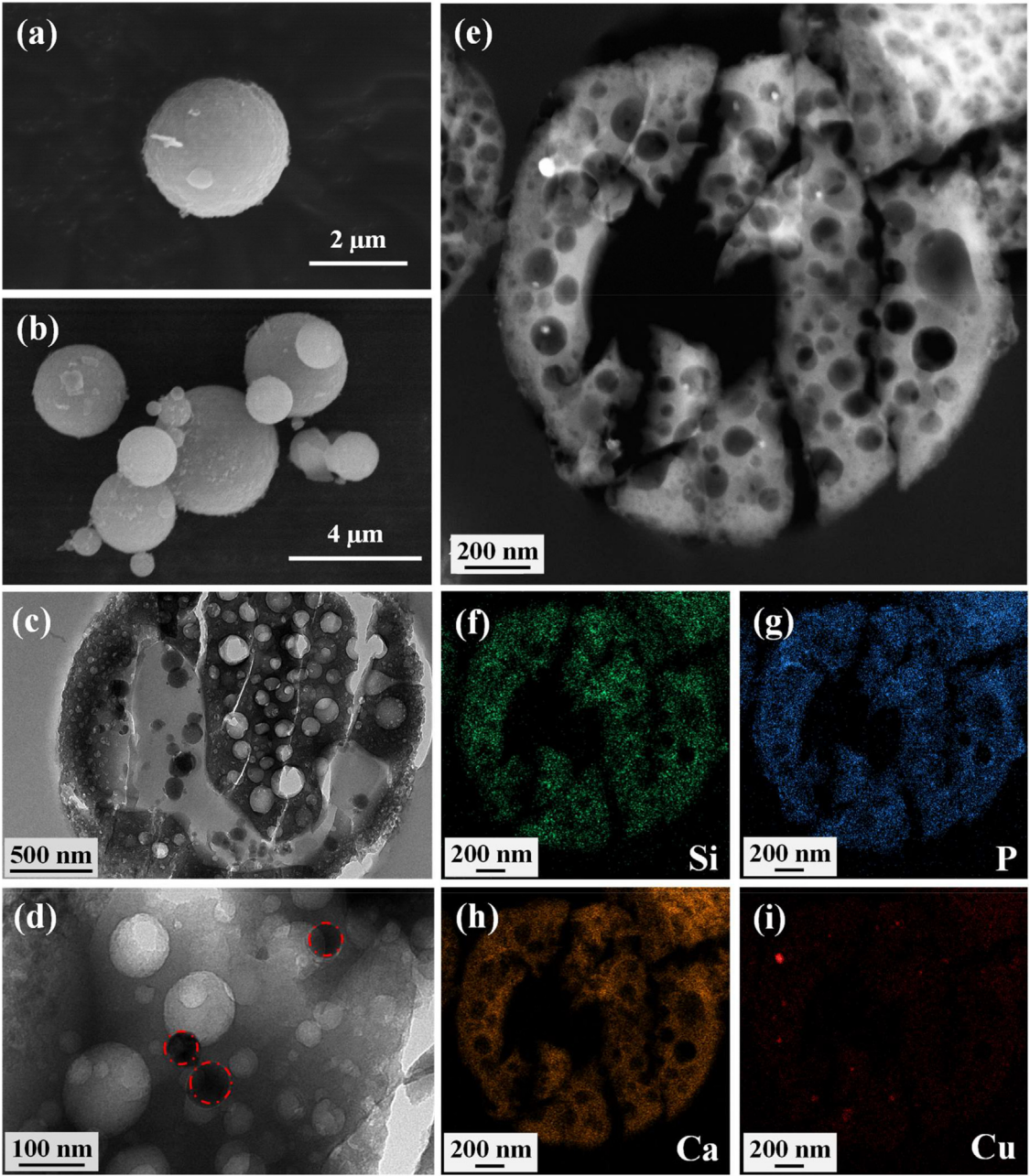


**Fig. 2.** SEM micrographs of individual (a) and group of as-synthesized particles (b) of 5-BG MPs; TEM images of the ultramicrotomed section of 5-BG MPs (c-d), red circles surrounding the Cu<sup>0</sup> nanoparticles; STEM-HAADF image of this section (e) and related STEM-EDX composition mapping of Si, P, Ca and Cu (f-i).

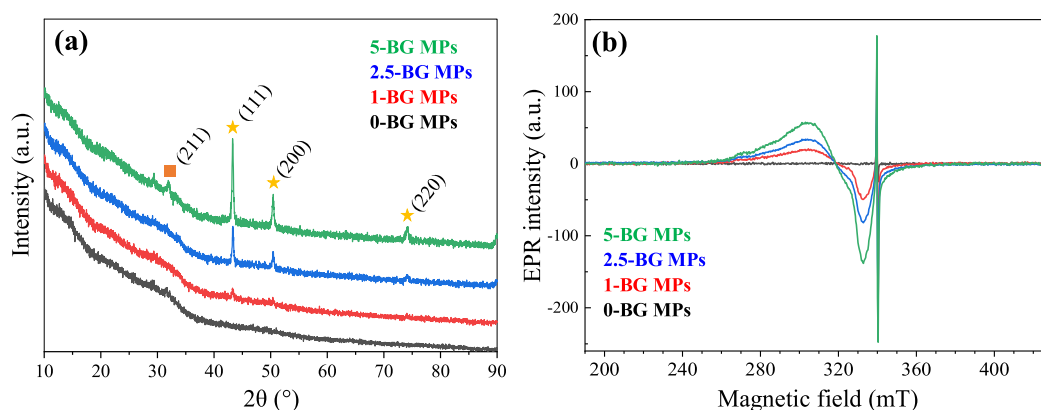


**Fig. 3.** XRD diffractograms (a) and EPR spectra (b) of spray-dried microparticles. The brown squares and yellow stars correspond respectively to nanocrystalline apatite and metallic copper  $\text{Cu}^0$ .

vaporization of unreacted TEP (215 °C) as its hydrolysis occurs at a very slow kinetics rate under acidic conditions [58]. This result confirms that the spray-drying technique allows the integration of all the bioglass precursors but without information on the spatial distribution of the latter inside the spheres.

With the aim to check the amorphous/crystalline nature of particles, XRD was carried out and is presented in Fig. 3-a. It reveals a broad halo centered around 30° and typical of amorphous silica network. It also shows the presence of a small amount of nanocrystalline apatite (major peak (211) at 31.8° /PDF 00-009-0432) for 0-BG MPs and 5-BG MPs samples. This phase is probably the result of partial crystallization during the thermal treatment (and limited by the silica matrix), as the pH in solution is too low to allow direct apatite formation [32]. Beyond apatite, diffraction peaks of metallic copper are detected at 43.3° (111), 50.5° (200) and 74.1° (220) (PDF 00-004-0836) [59]. Interestingly, the higher is the amount of Cu in the particles, the higher is the intensity of  $\text{Cu}^0$  peaks. The size of  $\text{Cu}^0$  crystallites ( $L_{\text{cryst.}}$ ) was also estimated by using the Debye-Scherrer formula [59,60] with the most intense peak 43.3° (111). The estimated sizes of crystallites (Table 1) are comprised between 60 nm and 70 nm. Therefore, XRD analysis demonstrates that: i) copper is integrated as  $\text{Cu}^0$  nanocrystals in particles, ii) the enhanced amount of crystalline  $\text{Cu}^0$  is not due to the increase of the nanocrystal sizes but to the increase of their number.

In order to fully understand and quantify how copper is involved in the particles, EPR spectroscopy was performed on the samples (Fig. 3-b). All EPR spectra exhibit two distinct signals labelled  $S_1$  and  $S_2$  associated with  $\text{Cu}^{2+}$  ions ( $3d^9$ ,  $S_{\text{eff.}} = 1/2$ ,  $I = 3/2$ ) and a sharp, intense and isotropic signal with a  $g$  value of  $2.0028 \pm 0.0002$  close to the free electron value of 2.0023. This last EPR signal may be due to free radicals [61] arising from the thermal decomposition of some TEOS or TEP residue or to conduction electrons associated with few-nanometre-sized metallic copper particles [62]. The  $S_1$  axial EPR signal with parallel and perpendicular components at  $g_{\parallel} = 2.35$  and  $g_{\perp} = 2.07$  and a partially resolved four-lines hyperfine structure ( $A_{\parallel} = 14.5$  mT and  $A_{\perp} < 0.5$  mT) is typical of isolated  $\text{Cu}^{2+}$  ions located at tetragonally distorted octahedral sites within a glassy network [63–65]. The broad and unresolved  $S_2$  signal observed at  $g \approx 2.1$  can be associated with  $\text{Cu}^{2+}$  ions in strong dipole-dipole interaction i.e. coupled  $\text{Cu}^{2+}$  pairs that can be associated to copper oxides  $\text{CuO}$  clusters for example [63,65].

The EPR intensity (obtained by double-integrating the EPR first-derivative curve) of both  $S_1$  and  $S_2$  signals clearly increases with the initial copper doping rate (Fig. 3-b) indicating that a part of  $\text{Cu}^{2+}$  ions were incorporated in the silica network. Furthermore, a

rough estimate of the  $\text{Cu}^{2+}$  content in the x-BG MPs ( $x = 1; 2.5; 5$  at.% Cu) samples was obtained by double-integration of the simulated  $S_1$  and  $S_2$  EPR signals (Figure S3) and comparison with reference compounds (mixed  $\text{CuSO}_4 \cdot 5\text{H}_2\text{O}$ -BN powders).

The EPR quantification results coupled with EDX results allowed to quantify the copper content involved in the different local environments in as-synthesized microparticles (Table 2-a): metallic copper  $\text{Cu}^0$ ,  $\text{Cu}^{2+}$  involved in the glassy network (isolated  $S_1/\text{Cu}^{2+}$ ),  $\text{Cu}^{2+}$  involved in  $\text{CuO}$  clusters (coupled  $S_2/\text{Cu}^{2+}$ ). It indicates that most of copper is integrated as metallic  $\text{Cu}^0$  (between 85.6 and 91.8 at.%), whereas between around 10 at.% is integrated as  $\text{Cu}^{2+}$  in the glassy network. Finally, a few percentages of copper are integrated in  $\text{CuO}$  environment. The latter is probably associated to nanometric clusters as no  $\text{CuO}$  phase is detected by XRD. Interestingly, there seems to be a threshold effect, as the percentage of  $\text{Cu}^0$  increases between 1-BG MPs and 2.5-BG MPs, whereas it decreases between 2.5-BG MPs and 5-BG MPs, to the benefit  $\text{Cu}^{2+}$  integrated in the glassy network.

TEM images of ultramicrotomed sections of the samples were recorded to investigate the inner part of particles. Images of 5-BG particles are shown in Fig. 2-c and d (pictures of the other samples are presented on Figure S1-b). The first important feature is that the particles exhibit an irregular inner porous structure beneath the superficial thin and dense shell. The "internal" nature of this porosity is confirmed by the low specific surface areas measured by  $\text{N}_2$  adsorption. The spherical pores have diameters ranging from few dozens to few hundreds of nanometres. In addition, some particles, regardless the Cu content, exhibit a hollow inner morphology. The reason of such particular internal structure must be sought in the combination of spray-drying process and thermal treatment. The precursor's solution at the outlet of the nozzle experiences fast evaporation kinetics of the solvent, from the surface to the center of the droplet. The high temperature and the increasing concentration inside each droplet enhance the hydrolysis/condensation reactions of the silica and phosphate alkoxide precursors with formation of ethanol and water as by-product. However, the speed of this process can induce chemical reactivity gradients. Hydrolyzed alkoxides located in the most peripheral part of the droplet will condense more rapidly earlier than those located in the central region. The latter will leave some of the precursors unreacted. This gradient in chemical reactivity can therefore lead to a porosity gradient: a denser zone at the periphery and a more porous zone in the centre. This may explain why only the larger particles show a hollow morphology, the gradient being less pronounced in the smaller particles. Subsequent heat treatment at 600 °C completes the condensation of the precursors, evaporating any remaining solvents and/or oxidizing counterions such as nitrates.



**Table 2**

Copper content involved in the different local environments in as-synthesized microspheres (a) and after 14 d of immersion in SBF: metallic copper Cu<sup>0</sup>, Cu<sup>2+</sup>involved in the glassy network (isolated S1/Cu<sup>2+</sup>), Cu<sup>2+</sup>involved in CuO clusters (coupled S2/Cu<sup>2+</sup>).

Sample	a-As-synthesized particles			b-Particles after 14 d in SBF		
	Cu <sup>0</sup> (at.%)	Cu <sup>2+</sup> <sub>network</sub> (at.%)	Cu <sup>2+</sup> <sub>CuO</sub> (at.%)	Cu <sup>0</sup> (at.%)	Cu <sup>2+</sup> <sub>network</sub> (at.%)	Cu <sup>2+</sup> <sub>CuO</sub> (at.%)
1-BG MPs	85.6 ± 0.1	12.5 ± 0.1	2.9 ± 0.1	84.0 ± 0.1	9.1 ± 0.1	6.9 ± 0.1
2.5-BG MPs	91.8 ± 0.1	7.7 ± 0.1	1.5 ± 0.1	92.7 ± 0.1	4.4 ± 0.1	2.9 ± 0.1
5-BG MPs	88.6 ± 0.1	10.4 ± 0.1	2.0 ± 0.1	70.5 ± 0.1	4.0 ± 0.1	25.5 ± 0.1

Another interesting detail of TEM images is that MPs sections of Cu-doped samples exhibit spherical nanoparticles darker than the surrounding MPs matrix, often located near the main cavity of hollow particles or individual smaller pores (Fig. 2-c/d). In order to check the nature of those NPs, we performed local STEM-HAADF image (Fig. 2-e) and STEM-EDX analysis of the 5-BG MPs particle's section (Fig. 2-f/g/h/i). As it can be seen from the quantitative analysis of the STEM-EDX mapping (Figure S4 and Table S2), copper is the main element of the brighter NPs observed in the STEM-HAADF images. This correlates with the darker NPs observed in the TEM images and the higher atomic number of copper which makes it heavier than that of the matrix element (zone 1 in Figure S4), and therefore more contrasting. STEM-EDX mapping of Cu shown in Fig. 2-i confirms the results. Therefore, STEM-EDX of the particle's section confirms EDX and EPR results, concluding that copper is mainly integrated inside the bioglass microsphere as reduced Cu<sup>0</sup> NPs. We hypothesize that copper nitrate clusters are formed during spray-drying and then undergo a chemical reduction to Cu<sup>0</sup> during the thermal treatment due to carbon residues from the pyrolysis of entrapped ethanol or non-hydrolyzed alkoxides remaining in the particles.

STEM-EDX mapping results in Fig. 2-g and h, Figure S4 and Table S2 reveal also the existence of Ca- and P-rich zones. These regions of a few dozen nanometres are mostly localized on porosity edges. Quantitative analysis performed on Ca/P rich and “matrix” zones verifies that the former exhibit a Ca and P amount much higher than the latter (localization, quantification and atomic ratios in Table S2). For Ca and P rich local zones, the Ca/P ratio of 1.37 or non-stoichiometric apatite with a high calcium deficiency is typical of amorphous calcium phosphates (ACP) [66].

In order to support the hypothesis of CaP clustering in the particle's matrix, and more generally the direct or indirect effect of the Cu content on the structural behavior of the silica network, the BG MPs were characterized by means of <sup>29</sup>Si, <sup>31</sup>P and <sup>1</sup>H solid-state NMR.

<sup>29</sup>Si MAS solid-state NMR (ssNMR) spectra with direct polarization (DP) are shown in Fig. 4-a, with all the typical resonances identified. Those resonances are relative to the different chemical species of Si described with the Q<sup>n</sup> nomenclature to highlight their connectivity and where *n* is the number of bridging oxygen atoms (BOs). The three-dimensional silicate network of bioactive glasses is mainly characterized by SiO<sub>4</sub> tetrahedra interconnected by four bridging oxygen atoms covalently bounded (Q<sup>4</sup>), that can be broken by a H atom (Si-OH) or by the inclusion of alkaline or alkaline-earth cations (Q<sup>3</sup> or lower) [67–69]. The network connectivity (NC) is an important structural parameter that is related to the stability of the silica network and thus to the bioactive glass reactivity [70,71]. The experimental NC is calculated from the percent of respective the Q<sup>n</sup> species contributing to the <sup>29</sup>Si resonance [68]:

$$NC = 1 \cdot Q_{Ca}^1 + 2 \cdot (Q_{Ca}^2 + Q_H^2) + 3 \cdot Q_H^3 + 4 \cdot Q^4 \quad (1)$$

Therefore, by increasing the number of non-bridging oxygens (NBOs) the contribution of lower species than Q<sup>4</sup> will increase, and consequently the network connectivity will decrease.

The <sup>29</sup>Si spectra of the bare BG MPs samples exhibit a predominance of the Q<sup>4</sup> species, with its chemical shift around −110 ppm. Other less-connected species can be distinguished depending on the chemical environment. It is demonstrated that in bioglasses with high amount of calcium the Q<sup>n</sup> species of Si-O<sup>−</sup> surrounded by Ca<sup>2+</sup> ions resonate at higher shifts with respect to silanol species (Si-OH) [53]. Typically, Q<sub>Ca</sub><sup>1</sup> and Q<sub>Ca</sub><sup>2</sup> resonate at −75 ppm and −83 ppm, respectively; Q<sub>H</sub><sup>2</sup> and Q<sub>H</sub><sup>3</sup> resonate at −91 ppm and −101 ppm, respectively. Q<sub>Ca</sub><sup>3</sup> and Q<sub>H</sub><sup>2</sup> overlap at the same chemical shift, so that it is impossible to separate the two contributions [72]. For the BG MPs samples all the Q<sub>x</sub><sup>n</sup> species were identified, with slight differences in their shifts depending on the Cu content probably due to Cu<sup>2+</sup> vicinity. All their contributions were deconvoluted (Figure S4), and the relative areas were summarized in Table S3 while the NC of each sample was calculated from Eq. (1) and reported in the graph in Fig. 4-b. The first clear difference is observed in 0-BG MPs, where Q<sub>Ca</sub><sup>1</sup> and Q<sub>Ca</sub><sup>2</sup> are not detected meaning that Ca<sup>2+</sup> ions are not involved in the silica network as network modifiers. This phenomenon could be explained by the different hydrolysis and then condensation kinetics of silicon and phosphorus alkoxides: most of hydrolyzed silicon alkoxides have condensed to form primary SiO<sub>2</sub> particles (also called clusters [53]) before spraying, whereas (hydrolyzed) phosphorus alkoxides could be still in solution as molecular species. This could lead to the association of calcium and phosphorus entities, leading to calcium phosphate and especially apatite or amorphous calcium phosphate after the calcination step. In a similar way the introduction of increasing amounts of copper in the solution leads to chelation between Cu<sup>2+</sup> and phosphates entities. As the coordination of copper is higher than the one of calcium, a part of the latter could interact with surface silanols of primary particles. During the final calcination step, this “remaining” calcium is then incorporated into the silicate network for Cu-doped glasses contrary 0-BG MPs. The integration of part of the copper into the glassy lattice, already demonstrated by EPR, is validated by ssNMR as Cu-doped samples show resonance bands slightly shifted towards higher values. This is because Cu<sup>2+</sup> ions interacting with NBOs cause resonance bands to shift and broaden [70,73].

<sup>31</sup>P DP MAS ssNMR spectra are shown in Fig. 5-a. The identified peaks correspond to the different phosphorous structural units, noted as Q<sup>n</sup><sub>P</sub>, where *n* is the number of bridging oxygens per phosphate tetrahedron [68,74]. The main peak at ~ 3 ppm represents orthophosphate tetrahedra associated with Ca<sup>2+</sup> ions (Q<sup>0</sup><sub>P</sub>) to form amorphous calcium phosphates (ACP) [66]. The identification of this resonance confirms that distinct ACP nanodomains are stabilized in the glass structure during the synthesis, as suggested by the detection of dense CaP zones in the EDX mapping of 5-BG MPs. Two broader resonances are observed at around −8 ppm and −23 ppm, much more pronounced in Cu-doped samples. Their broadness can be related to structural heterogeneities or possibly a faster T<sub>2</sub> relaxation linked to presence of paramagnetic Cu<sup>2+</sup> ions. The first band may likely be ascribed to the resonance of isolated PO<sub>4</sub> units (Q<sup>1</sup><sub>P</sub>) bonded to the silica network (P-O-Si) or dimeric phosphates (Q<sup>1</sup><sub>P</sub>), and the second to tripoly-phosphates (Q<sup>2</sup><sub>P</sub>) [75,76]. All the Q<sup>n</sup><sub>P</sub> species were decomposed and presented



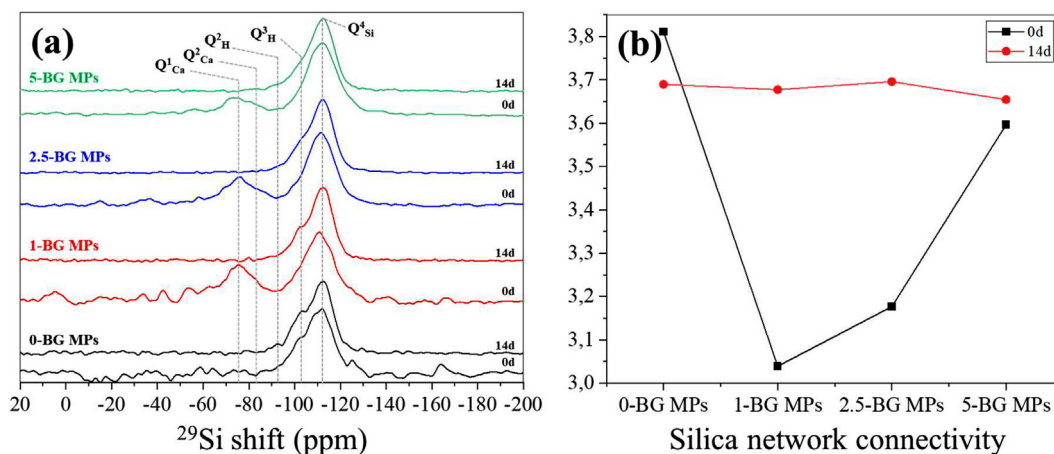


**Fig. 4.**  $^{29}\text{Si}$  MAS solid state NMR spectra (a) and silica network connectivity (NC) (b) of the spray-dried BG MPs before and after 14 d of immersion in simulated body fluid (SBF).

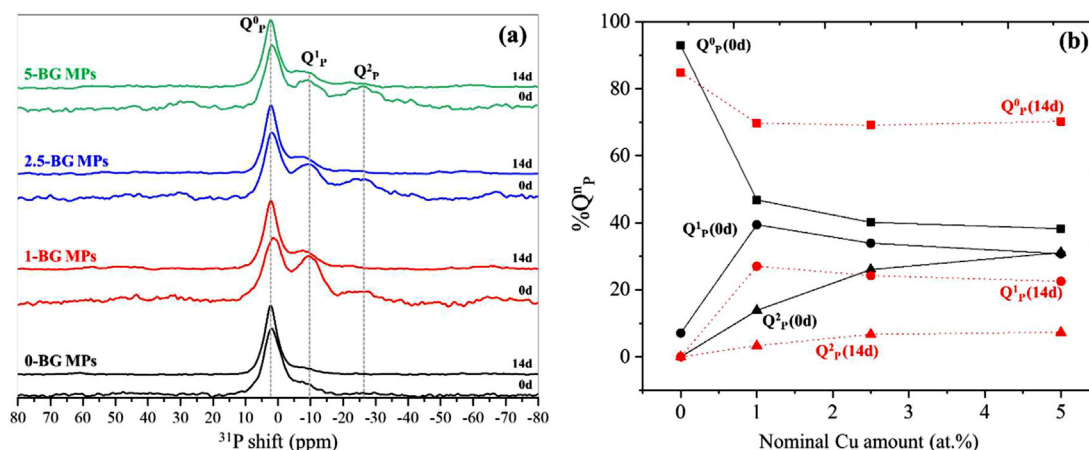


**Fig. 5.**  $^{31}\text{P}$  MAS solid state NMR spectra of the spray-dried BG MPs before (0 d) and after 14 d of immersion in simulated body fluid (SBF) (a); percentage of the  $Q^n_P$  species present in the BG MPs samples as a function of the Cu content, both before (0 d) and after 14 d of immersion in SBF (b).

in Figure S5 while the evolution of the percentage of each entity ( $Q^0_P/Q^1_P/Q^2_P$ ) as a function of Cu doping amount is presented in Fig. 5-b. The copper integration in the BG-MPs increases significantly the  $Q^1_P$  species contribution (dimeric calcium pyrophosphates and individual orthophosphates groups bounded with silica), while the  $Q^2_P$  resonance appears (tripoly-phosphates). Moreover, the sum of  $Q^1_P + Q^2_P$  increases with the Cu content, but  $Q^2_P$  increases at the expense of  $Q^1_P$ .

These results clearly demonstrate that the presence and the amount of copper affect the way the phosphates are integrated in microspheres. For non-doped 0-BG MPs, most of phosphate ions are involved in amorphous calcium phosphate (ACP) rather than participating to the silicate network (Fig. 5-a). It is consistent with the low contribution of  $Q^1_{Ca}$  and  $Q^2_{Ca}$  of silicate species for 0-BG MPs (Fig. 4-a) as  $\text{Ca}^{2+}$  is associated to orthophosphates. As stated previously, the presence of copper in the pre-spraying solution leads to chelation between  $\text{Cu}^{2+}$  and phosphates entities for 1-BG MPs, 2.5-BG MPs and 5-BG MPs samples. Contrary to  $\text{Ca}^{2+}$ ,  $\text{Cu}^{2+}$  is reduced into  $\text{Cu}^0$  during the calcination step. We can hypothesize that the phosphate ions that previously interacted with copper are integrated in the silicate network as dimers or trimers in the close vicinity of  $\text{Cu}^0$  nanoparticles. It could also explain the evolution of the silicate network connectivity (NC) as a function of copper amount (Fig. 4-b). NC is high for the non-doped sample because most of calcium is associated to phosphate and does not act as silica network modifier. When copper is added (1-BG MPs),

a part of the calcium is incorporated in the network, decreasing the connectivity. Nevertheless, the latter is increased when increasing the amount of copper (2.5-BG MPs and 5-BG MPs). Indeed, as long as calcium is considered to be “substituted” by copper in the nominal formulation, the  $\text{Ca}^{2+}$  involved as network modifier is decreased leading to an enhanced NC, whereas Cu is incorporated to metal copper nanoparticles.

$^1\text{H}$  MAS ssNMR spectra are shown in Figure S6. The main peaks of the synthesized samples were identified with different OH species and with the presence of  $\text{H}_2\text{O}$  in different forms [66]. The first broad resonance at  $\sim 5$  ppm was attributed to both physisorbed and structural water and silanol groups engaged in weak-hydrogen bonds. The rapid decrease of the band from 0-BG MPs to 5-BG MPs is directly correlated to the preponderance of ACP domains in ternary MPs with respect to the Cu-doped samples. In fact, it is well-known that significant amount of water is involved in the formation of amorphous calcium phosphates [77]. The second peak at  $\sim 2$  ppm corresponds to isolated silanol groups, and it decreases with the increasing of Cu amount. It could be due to the condensation of silanol with phosphate entities during the copper reduction (calcination step). Multiple weak and narrow signals are detected in the 0.8–1.5 ppm region, that belong to water molecules terminating the c-channels of  $\text{OH}^-$  groups in the hydroxyapatite structure [78]. In addition, their intensities are directly proportional to the nanocrystalline apatite (nHA) structural disorder [78]. Another sharp peak belonging to the superficial ACP

anions  $\text{OH}^-$  resonates at  $\sim 0$  ppm. Nanocrystalline hydroxyapatite in bare samples has already been detected by XRD analysis, and it stems from partial recrystallization at high temperature [32], but its presence will be discussed in detail in the bioactivity section.

The FTIR spectra of the synthesized Cu-BG MPs are shown in Figure S7. There are no particular differences between the four samples arising from the spectra. All of them exhibit the typical absorption bands of the silica network, identified by comparing them with the results in literature [79–81]. The bands at  $1100\text{ cm}^{-1}$ ,  $815\text{ cm}^{-1}$ ,  $466\text{ cm}^{-1}$  correspond, respectively, to the asymmetric stretching, bending, and rocking vibrations of the siloxane bond (Si-O-Si). The band at  $1633\text{ cm}^{-1}$  belongs to the O-H bending mode of physically adsorbed water. The wide band at  $3430\text{ cm}^{-1}$  and the small shoulder at  $940\text{ cm}^{-1}$  are, respectively, the stretching and bending vibrations of the hydrogen bonded silanol groups (Si-OH...H<sub>2</sub>O). At  $604\text{ cm}^{-1}$  and  $564\text{ cm}^{-1}$  two small peaks can be observed, standing for the bending and stretching vibrations of  $\text{PO}_4^{3-}$  ions in a CaP environment, both apatitic and non apatitic [82–84]. The presence of calcium phosphates phases confirms the  $^{31}\text{P}$  MAS ssNMR results, where ACP and HA are detected. Apatite detection also confirms the weak diffraction peaks found in 0-BG MPs and 5-BG MPs.

### 3.2. Acellular in vitro evolution in SBF

The acellular “bioactivity” of Cu-doped bioglass microspheres was assessed by immersing the powders in simulated body fluids model solution for predetermined time-points, from 1 h to 14 d. Then the resulting powder was separated from the SBF solution, washed with ultrapure water, dried at  $60^\circ\text{C}$  and characterized.

SEM micrographs of individual and agglomerated MPs after 14 d of degradation are presented in Fig. 6, while images of MPs after shorter periods of immersion in SBF, 24 h and 7 d, are shown in Figure S8. Whatever the initial composition of samples, individual particles (Fig. 6-b/d/f/h) increase their superficial roughness at 14 d with respect to bare particles, with formation of needle-like crystals typical of HA phase nucleating on bioglass surface. Samples soaked in SBF for 14 d do not exhibit significant morphological changes with respect to the particles at 7 d (Figure S7). However, “individual” MPs do not represent statistically the behavior of most of MPs when immersed in SBF, even if they are useful to display the typical morphology of apatite crystals in a simplified way. In fact, most of the particles are arranged in large aggregates covered of an irregular hydroxyapatite multilayer.

By observing the micrographs of MPs groups (Fig. 6-a/c/e/g), particles exhibit a tendency to strongly aggregate, unlike unsoaked MPs that are more dispersed. Those agglomerations of particles display the “cauliflower” morphology typical of the surface-nucleated HA [85], starting from 24 h of immersion. In addition, the apatite layer formed on the surface of MPs aggregates and in the interstices between particles grows over time, especially between 24 h and 7 d. On the contrary, there are not relevant morphological differences detected among the four BG MPs samples.

In order to better understand the compositional changes occurring in the BG MPs powders while they are soaked in SBF, SEM-EDX analysis was performed on the samples after 14 d of degradation. Samples compositions of the major oxides ( $\text{SiO}_2$ ,  $\text{P}_2\text{O}_5$ , CaO, CuO) are reported in Table S5 in comparison to those at 0 d.

EDX analysis results show for all the samples a relevant decrease of the  $\text{SiO}_2$  content (up to  $-4.8\%$  for 5-BG MPs) due to the degradation of the silica network and to the solubilization of  $\text{SiO}_4^{4-}$  ions. The slight increase of  $\text{P}_2\text{O}_5$  (up to  $+0.5\%$  for 5-BG MPs) and the larger increase of the CaO content (up to  $+5.4\%$  for 5-BG MPs) suggest that after 14 d calcium and phosphorus are integrated from the medium to form HA nanocrystals at the microspheres’ surface. After 14 d, the Ca/P ratios are 5.87, 4.29, 3.77

and 3.25 for 0, 1, 2.5 and 5 % Cu-doping respectively. As expected, the CuO fraction of the synthesized glasses after 14 days is lower than that at  $t_0$ , due to the release of  $\text{Cu}^{2+}$  ions following the decomposition of the glass structure.

The changes in the glass structure of the spray-dried MPs after soaking in SBF for 14 d were investigated by  $^{29}\text{Si}$ ,  $^{31}\text{P}$  and  $^1\text{H}$  MAS ssNMR. Possible shifts of the main peaks, broadening of the bands and changes in the single contributions after deconvoluting the spectra are discussed.

The main considerable alteration of  $^{29}\text{Si}$  spectra (Fig. 4-a) is the fading of the  $Q^1_{\text{Ca}}$  and  $Q^2_{\text{Ca}}$  signals at  $-75$  ppm and  $-83$  ppm, respectively. Spectra decompositions (Figure S5), show that the intensity of  $Q^2_{\text{H}}$  and  $Q^3_{\text{H}}$  species was reduced, at the benefit of  $Q^4_{\text{Si}}$  species. Moreover, the calculated NC for the BG MPs samples at 14 d are higher with respect to 0 d. The decreasing of  $Q^1$ ,  $Q^2$ , and  $Q^3$  contributions is explained with the rapid release of metal cations (mainly  $\text{Ca}^{2+}$  and a part of  $\text{Cu}^{2+}$ ) in the medium in the early hours of immersion in SBF, followed by a partial depolymerization effect of silica surface. The repolymerization observed at 14 d (increase of NC) is due to a partial condensation of the silicic acid ( $\text{Si}(\text{OH})_4$ ) that repolymerizes, but also as an indirect effect of the metal cations release, that reduces the contributions of  $Q^1_{\text{Ca}}$  and  $Q^2_{\text{Ca}}$  species. These results showing the disappearance of the calcium involved in the silicate network combined with the homogeneous spatial distribution of the calcium in particle (Fig. 2-h) demonstrate that the initial inner porosity has been connected to the fluids during the interaction with SBF (via partial degradation) to allow the full  $\text{Ca}^{2+}$  leaching from the glass network.

$^{31}\text{P}$  spectra (Fig. 4-a) are quite different for initial samples and after immersion in SBF during 14 d. The evolutions of ( $Q^{\text{p}}_{\text{p}}$ ) percent as the nominal copper amount are presented in Fig. 4-b. For the 0-BG MPs sample after 14 d of immersion, most of phosphate entities are involved in calcium phosphate (orthophosphate tetrahedra associated with  $\text{Ca}^{2+}$  ions  $Q^0_{\text{p}}$ ), and almost no ( $Q^1_{\text{p}}$ ) nor ( $Q^2_{\text{p}}$ ) are observed similarly to the sample at  $t_0$ . The negligible evolutions of these percentage values from 0 to 14 d can however be correlated with local environment evolution. In fact, previous works show that the orthophosphate peak at  $\sim 3$  ppm can be split in two contributions: a broad and Gaussian signal indicating a structural CaP disorder and thus belonging to the ACP phase; and a narrow signal represented by a Lorentzian function that is associated to structural order of calcium phosphates, and thus the nHA phase [77,86]. In our case, because of multiple contributions it was difficult to clearly deconvolute this peak [87]. Contrary to 0-BG MPs, Cu-doped samples demonstrate important differences between 0 d and 14 d. Amounts of ( $Q^2_{\text{p}}$ ) entities are strongly decreased, probably because of the easy hydrolysis of P-O-P bonds. ( $Q^1_{\text{p}}$ ) is also decreased due to the Si-O-P hydrolysis and the release of phosphates in the medium. The increase of ( $Q^0_{\text{p}}$ ) at the expense of both ( $Q^1_{\text{p}}$ ) and ( $Q^2_{\text{p}}$ ) “network phosphate” demonstrate the formation of calcium phosphate and potentially apatite. Two mechanisms could lead to nHA formation: i) the evolution of initial ACP into nHA with close chemical composition, maintaining the morphology and spatial distribution in the microspheres, ii) the recombination of  $\text{Ca}^{2+}$  and  $\text{PO}_4^{3-}$  ions from the medium (initially present or released from particles) and the subsequent reprecipitation of apatite nanocrystals. Considering the large enhancement of ( $Q^0_{\text{p}}$ ) from almost 50 % to 70 %, and the enhancement of Ca and P detected by EDX (Table S5) both mechanisms should be involved.

$^1\text{H}$  MAS NMR spectra after 14 d presented in Figure S6 show the reduction of the superficial ACP  $\text{OH}^-$  at 0 ppm and a slight increase of multiple weak and narrow signals detected in the 0.8–1.5 ppm region (water molecules terminating the c-channels of  $\text{OH}^-$  groups of hydroxyapatite). These changes qualitatively demonstrate the nHA formation associated to a remarkable increasing of the signal at 5 ppm. the  $^1\text{H}$  signals at 5 ppm are

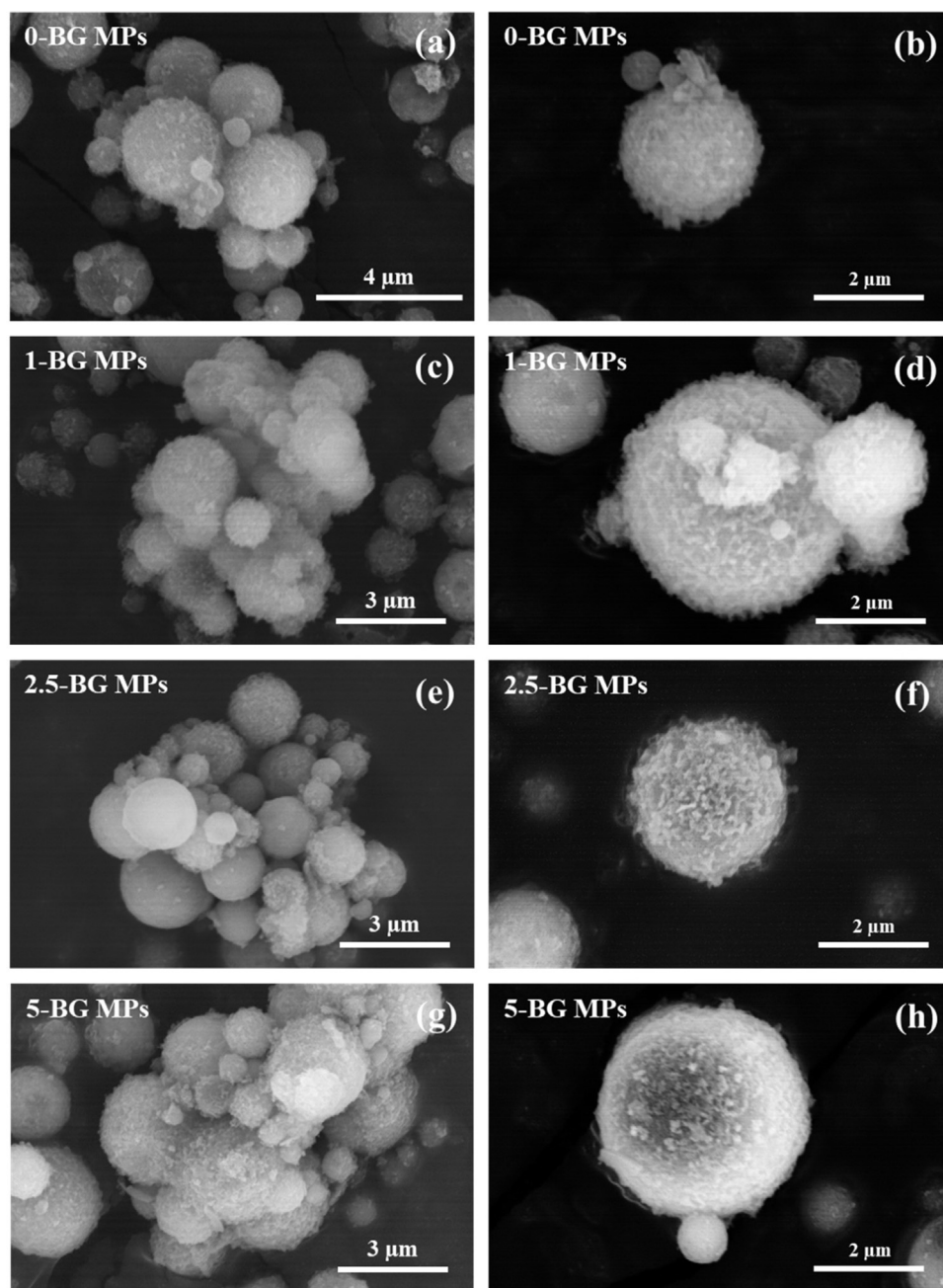


**Fig. 6.** SEM micrographs of agglomerated (a, c, e, g) and individual (b, d, f, h) particles of the synthesized BG MPs samples after 14 days of soaking in SBF.

broad (except for 0-BG-14d), so they seem associated with water molecules with low mobility (structural water). Presence of free water cluster would sharpen the resonance.

Differently, the peak at 2 ppm belonging to the isolated silanol groups decreases as an effect of the silica re-polymerization usually described as a step of bioactive glass reactivity [1].

$^1\text{H} \rightarrow ^{29}\text{Si}$  and  $^1\text{H} \rightarrow ^{31}\text{P}$  CP MAS ssNMR spectra (Figure S9 and S10) arise from the dipolar-coupling-mediated magnetization transfer from H atoms to  $\text{Q}^n\text{Si}$  and  $\text{Q}^n\text{P}$  species, thus identifying  $^{29}\text{Si}$  and  $^{31}\text{P}$  nuclei adjacent to H atoms in the structure [88,89]. In our samples, the clearest differences for  $^{29}\text{Si}$  CP MAS ssNMR between 0 d and 14 d samples are as for the DP  $^{29}\text{Si}$  experiments the disappearance of  $\text{Q}^1\text{Ca}$  and  $\text{Q}^2\text{Ca}$  signals but also the exacerbation of  $\text{Q}^3\text{H}$  species. It confirms the relevant water uptake during the immersion in SBF, with formation of protonated species. For  $^{31}\text{P}$  CP

MAS ssNMR, an increase of  $\text{Q}^1\text{P}$  and  $\text{Q}^2\text{P}$  signals is observed which seems to be the opposite of what is seen by DP  $^{31}\text{P}$  experiment. The most likely explanation is associated with the release of paramagnetic  $\text{Cu}^{2+}$  ions. Indeed, the presence of these at 0 d greatly reduces the efficiency of H-P polarization transfer due to the rapid relaxation mechanism giving weak CP signals for 0 d which are restored at 14 d with the release of the  $\text{Cu}^{2+}$ .

The evolution of the structure was also investigated by FTIR spectroscopy and XRD, and the spectra and x-ray diffractograms from each time-point (from 0 d to 14 d) were stacked to better understand the changes over time. FTIR and XRD results of 0-BG MPs, 1-BG MPs, 2.5-BG MPs and 5-BG MPs are shown in Figure S11, S12, S13 and S14, respectively. In FTIR spectra of the BG MPs samples, all the bands belonging to the silica network remained unchanged. Instead, the  $\text{PO}_4^{3-}$  band ( $500\text{--}650\text{ cm}^{-1}$ ) increased its



intensity progressively, until two distinct peaks appeared at  $604\text{ cm}^{-1}$  and  $564\text{ cm}^{-1}$ . Those peaks partially correspond to the vibration bands of the orthophosphate groups in apatitic environments, and therefore they constitute a qualitative evaluation of nHA formation. Another small peak at  $880\text{ cm}^{-1}$ , corresponding to the vibration of  $\text{CO}_3^{2-}$  group, could correspond to the formation of carbonated nano-hydroxyapatite (nHCA) [90]. While for the ternary particles (0-BG MPs) the two orthophosphate vibrations appeared since the first hours of immersion, for Cu-doped samples the two bands started to be distinguished from 24 h (1-BG MPs) or from 6 h (2.5-BG MPs and 5-BG MPs). Then, Cu-doped bioglass microspheres exhibit a delayed formation of hydroxyapatite with respect to the undoped sample. This phenomenon could be explained considering a balance between the two mechanisms previously mentioned i.e. ACP transformation vs. nHA nucleation from ions of SBF.

Formation of the nHA is also confirmed by XRD analysis, with the emergence of peaks at  $25.9^\circ$  (102) and  $31.8^\circ$  (211) and their gradual increase with time. In addition, nHA peak appears more pronounced starting from 1 h in ternary MPs, while in 1-BG MPs from 24 h and in 2.5-BG MPs and 5-BG MPs from 6 h. Regarding the presence of metal copper  $\text{Cu}^0$  phase, the average crystallite size was calculated after 14 d of degradation (Debye-Scherrer / (eq. 2). Results are plotted in Figure S15. No relevant differences in crystallites size are detected for the Cu-doped samples after 14 d.

Besides nHA and  $\text{Cu}^0$  phases, the occurrence of peaks belonging to calcium carbonate crystals ( $\text{CaCO}_3$ ), and in particular the calcite phase (PDF 00–005–0586) are also detected, with its most intense peak at  $29.4^\circ$ . In addition, not all the time-point diffractograms exhibit  $\text{CaCO}_3$  but only at 3 h, 6 h, 7 d and 14 d. It must be considered that SBF is a metastable saline solution, containing a relevant concentration of both calcium and carbonate ions, so that their crystallization is likely to occur. Calcite crystals were found in previous research works [32,91–93] their nucleation is more likely to occur in the first soaking hours. In 0-BG MPs and 1-BG MPs the peaks appear starting from 6 h of immersion. In 5-BG MPs they are detected only at 1 h of soaking, while in 2.5-BG MPs they are not detected at all, showing that this event could be due local supersaturation associated to aggregation of microspheres. Although the nucleation of calcite crystals cannot be avoided, their amount is probably limited since its presence is not detected in FTIR spectra, and thus their existence does not affect the bioactivity of the synthesized bioglass microspheres [93].

Combination of EPR spectroscopy (Figure S16) and EDX performed on microspheres after 14 d of interaction with SBF allowed to check the evolution of copper environment. Results are summarized in Table 2-b. Concerning  $\text{Cu}^0$ , there was little change for 1-BG MPs and 2.5-BG MPs between the as-synthesized samples and after 14 d of interaction (around 84 and 92 at.% respectively). However, for these two samples, the proportion of  $\text{Cu}^{2+}$  integrated into the silicate lattice decreases (to the benefit of  $\text{Cu}^{2+}$  associated with  $\text{CuO}$ ), suggesting that most of the copper released comes from the silicate network. Contrary to the other samples, 5-BG MPs demonstrates a significant decrease of  $\text{Cu}^0$  percentage that can be linked to the threshold effect previously described for the integration of copper in the as-synthesized particles. In the same time there is a significant increase of  $\text{Cu}^{2+}$  involved in  $\text{CuO}$  highlighting the potential surface oxidation of a part of metallic copper nanoparticles during the immersion in SBF.

#### Ion release profile and pH evolution

Ionic profiles of the spray-dried bioglass microspheres were determined by ICP-OES for Si, P, Ca and Cu elements, by analyzing the SBF solutions from 1 h to 14 d, including the initial SBF solution. Results are grouped by element and are shown in Fig. 7, with a zoom on the right for the first time-points (0 d, 1 h, 3 h, 6 h).

All the samples exhibit a similar trend of each element releasing, even with few differences in the concentration values.

Si profile (Fig. 7-a), that is not initially present in SBF, shows a rapid release in the first hour of immersion, in the range 70–90 ppm. Next, it begins to slightly decrease until 7 d, after which it remains constant. Calcium concentration (Fig. 7-c) initially follows a similar burst effect, from about 100 ppm at 0 d to 300–330 ppm at 1 h, depending on the sample. However, after staying constant for the following hours, the  $\text{Ca}^{2+}$  dissolved undergoes a drastic decrease, almost reaching the same initial values. After that, it rises back to almost the values of the burst effect (260–300 ppm depending on the sample), and then plateaus. On the contrary, P dissolved in solution, undergoes continuous decrease until it is no longer detected starting from 24 h of soaking (Fig. 7-b). Finally, Cu profile (Fig. 7-d) of Cu-doped samples exhibits a burst effect in the first hour with respect to Si and Ca trends (8 ppm for 1-BG MPs, 17 ppm for 2.5-BG MPs and 5-BG MPs). After that time, Cu concentration of 1-BG MPs and 2.5-BG MPs does not change significantly, while for 5-BG MPs the amount of copper in solution continues to increase up to 25 ppm at 7 d.

The mineralization process of bioactive glasses immersed in SBF involves a complex mechanism of ion exchange between surface and medium. As the silica network starts to degrade, active cations such as  $\text{Ca}^{2+}$  and  $\text{Cu}^{2+}$ , but also anions such as  $\text{SiO}_4^{4-}$  and  $\text{PO}_4^{3-}$  (and their protonated forms) are released in the medium. Then, being the SBF solution supersaturated regarding hydroxyapatite phase,  $\text{Ca}^{2+}$  and orthophosphate ions ( $\text{PO}_4^{3-}$  and  $\text{HPO}_4^{2-}$ ) reprecipitate on the bioglass surface and recombine to form amorphous and/or (poorly) crystalline calcium phosphates. By considering the ionic release profiles and the results of the powder characterization, the behavior of the synthesized BG MPs globally follow the same trends than models described by L. Hench and co-workers [94–96], and in previous works [92], but with some modifications.

In the early stage of immersion in SBF, two events occur consequently and almost simultaneously. Firstly, once the medium enters in contact with the BG MPs surface, a large amount of  $\text{Ca}^{2+}$  and  $\text{Cu}^{2+}$  cations diffuse through the silica structure and pass in solution. Cation vacancies are promptly replaced by  $\text{H}^+$ ,  $\text{H}_3\text{O}^+$  and  $\text{H}_2\text{O}$ , which attack the silica network (both bridging and non-bridging oxygen atoms) by hydrolyzing the siloxane bond  $\text{Si-O-Si}$  and creating silanol groups. Interestingly, 1-BG-MPs and 2.5-BG-MPs demonstrate the highest rate of released Si and Ca between 1 h and 6 h. It is clearly related with the lowest network connectivity (NC, Fig. 4-b) of this sample. It is correlated with the larger amount of  $Q^1_{\text{Ca}}$  and  $Q^2_{\text{Ca}}$  silicon environment leading to enhanced silica network hydrolysis. Then, during this step, silica dissolves in SBF in the form of silicic acid  $\text{Si}(\text{OH})_4$  or longer oligomers. The consequence of this ionic exchange, besides the high Si release, is the sudden increase of the pH (Figure S17) in the first hour, from 7.4 up to 8–8.25 depending on the sample. The confirmation that the silicon release is responsible for the pH increase is given by their directly proportional relation. In fact, 1-BG MPs, that releases the highest content of  $\text{Si}(\text{OH})_4$  groups, exhibits the highest pH increase, so as for the other samples that follow the same relation.

Between 1 h and 6 h, the concentration of Si, Ca and Cu in SBF remains globally constant, while P keeps lowering. During these hours the reprecipitation process begins, but slowly, since it is still balanced by the fast releasing of the elements.

Orthophosphate groups do not follow the same behaviour probably because contrary to the  $\text{Ca}^{2+}$  that is a network modifier enhancing degradation of silica and totally leached out from the silica network at the end of interaction (Fig. 4-a), phosphorus is a network-former, covalently integrated in the silica network. As demonstrated by Fig. 5-b, almost 25% of phosphorus is still present after 14 d in the silica network (the  $\text{Si-O-P}$  bond associated to



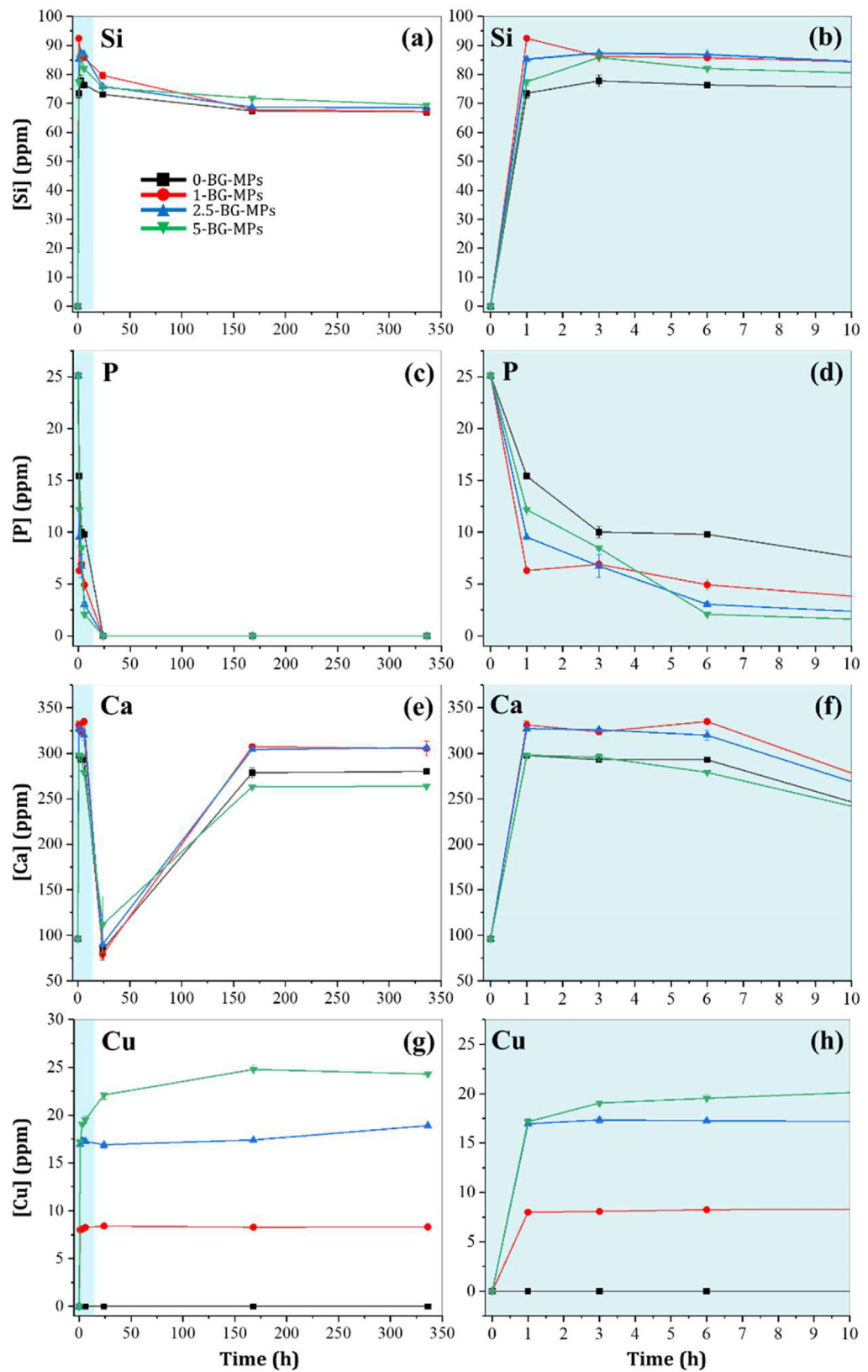


**Fig. 7.** Ion release profile of the spray-dried BG MPs during *in vitro* acellular tests in SBF, from 0 d to 14 d. The graphs on the right represent the zoom of the first time-points (0 d, 1 h, 3 h, 6 h). Every point in the graphs corresponds to the concentration of the element (Si, P, Ca or Cu) detected in SBF solution at each time-point. The error bars are present for each point but sometimes too small to be clearly visible.

( $Q^1_p$ ) species). As this phosphorus is still involved in the particles, the formation of calcium phosphate requires phosphates from the medium. Indeed,  $Si(OH)_4$  groups condensate forming a silica-rich porous layer, on which calcium and phosphate precipitate giving mostly amorphous calcium phosphates and/or non-stoichiometric apatite heterogeneously distributed as it can be observed from SEM micrographs at 24 h. The MPs' surface is not totally covered of those species, and this may be the reason of the constant concentration of Si and Ca in SBF between 1 h and 6 h. Indeed, undergrated regions of particles allow a high dissolution rate that still compensates the ionic loss due to their precipitation. As the apatite continues to deposit and crystallize on the BG surface,  $SiO_4^{4-}$  and  $Ca^{2+}$  diffusion starts to decrease, and that can explain why calcium concentration collapses to the initial level in SBF within 24 h, while phosphates are no longer detected. Between 6 h and 24 h the apatite precipitation accelerates and spreads over the MPs surface together with the silica amorphous layer, so that the Si and Ca lowering in the medium is the result of their difficulty to diffuse through those new phases/layer. FTIR spectroscopy and XRD results sustain this hypothesis, since the presence of apatite starts to be sufficiently detected within the first 24 h of immersion. As the phosphate amount in SBF runs out after 24 h,  $Ca^{2+}$  concentration turns back to increase up to 7 d, then its kinetics becomes static, as well as for the  $SiO_4^{4-}$  ions. The unavailability of phosphate groups in the medium prevents  $Ca^{2+}$  ions from recombining and precipitating, so their presence in solution continues to increase. However, ACP nanodomains in the inner part of particles are exposed to water uptake, the latter following new diffusion pathways created by the partial silica degradation and the intrinsic inner porosity of spray-dried microspheres. Consequently, ACP clusters evolve toward nHA crystals according to the mechanism described above and proved by FTIR and XRD results. Furthermore, the gradual decrease of the pH from 24 h to 14 d suggests that  $OH^-$  ions are progressively absorbed within the apatite structure, which turns into nanocrystalline hydroxyapatite. Therefore, the static kinetics of releasing exhibited by all the elements and for all the samples is to be considered only apparent. In reality, an equilibrium between ions diffusion through the BG structure ( $SiO_4^{4-}$ ,  $PO_4^{3-}$  and  $Ca^{2+}$ ) and their precipitation is reached, and the consequence is the gradual growing of the nHA phase. In this last period,  $HCO_3^-$  and  $CO_3^{2-}$  are absorbed into the HA structure, forming a nHCA phase, as already mentioned in the FTIR analysis.

The copper release curves (Figure S18) were fitted with the following model:  $[Cu^{2+}] = k \cdot t^n$  (where  $t$  represents time,  $k$  is the rate constant of the reaction, and  $n$  is the order of the reaction) to quantitatively compare copper release kinetics. The values of  $k$  increase with the initial dopant quantity in the glasses, with respective values of 8.08567, 16.82993, and 16.82993 for 1-BG MPs, 2.5-BG MPs, and 5-BG MPs. The values of  $n$  also increase, with respective values of 0.00593, 0.01282, and 0.06084. Copper release behavior can be understood only by investigating how it was integrated in the glass network. Indeed, as demonstrated by EPR and XRD copper could be either reduced in  $Cu^0$  nanoparticles, integrated in the silica network as  $Cu^{2+}$  ions or less frequently in  $CuO$  clusters. The maximum  $Cu^{2+}$  released amount corresponds to 24.6 %, 18.8 % and 16.9 % of the total copper integrated in 1-BG MPs, 2.5-BG MPs and 5-BG MPs, respectively. Considering the respective percentage evolution of each Cu environment (Table 2-a and b), the copper released in SBF mainly comes from the glass network and to a lesser extent from  $Cu^0$  nanocrystals. This behavior is particularly interesting because the remaining copper stocked as  $Cu^0$  could provide long term antibacterial and pro-angiogenic effect [24].

Beyond this direct structural effect of copper doping, the latter also impacts the calcium and phosphorus integration either in CaP nanodomains or in the silica network. This consequence in-

fluences the silica network connectivity and the release kinetics of major species ( $SiO_4^{4-}$ ,  $PO_4^{3-}$ ,  $Ca^{2+}$ ), and subsequent calcium phosphate precipitation and doping ions ( $Cu^{2+}$ ). This tunable behavior is a key factor for the understanding of further biological effects, since these ions play a fundamental role in the bone neoformation process, antibacterial activity potential cytotoxicity-related issues.

#### 4. Conclusion

This study presents a pioneering approach in synthesizing Cu-doped ternary silica-based bioactive glass microspheres using a combination of sol-gel chemistry and spray-drying technique. The resulting microparticles are well-defined and non-aggregated with spherical shapes and diameters of a few microns. They exhibit inner porosity, the latter being intrinsic of the spray-drying process and due to rapid solvent evaporation.

The effects of copper-doping on the structure and composition of microspheres have been thoroughly described at different scales through complementary advanced techniques. For all doped samples, copper is incorporated in microspheres mainly in the form of  $Cu^0$  nanoparticles (formed by reduction with carbon from the pyrolysis of entrapped organic species) and is also integrated into the amorphous matrix as  $Cu^{2+}$ . Beyond this direct effect, copper-doping impacts the connectivity of the silica network as demonstrated by  $^{29}Si$  solid state NMR measurements. Indeed, whereas  $Q_{Ca}^1$  and  $Q_{Ca}^2$  are detected for Cu-doped particles meaning that calcium is involved as silica network modifiers, they are not for the undoped particles, calcium being associated with phosphorus in amorphous calcium phosphate nano-domains.  $^{31}P$  NMR results confirm these conclusions in particular with the decrease of  $Q^0_p$  associated to calcium phosphates at the advantage of  $Q^1_p$  orthophosphates and/or  $Q^2_p$  tripolyphosphates, these latter participating to the glassy network. This different behavior is supposed to be induced by preferential  $Cu^{2+}$  and phosphates entities complexation during the pre-spraying step. These results clearly demonstrate that the presence and the amount of copper affects the way copper, phosphate and calcium elements are integrated in microparticles. Logically, these differences affect the amplitude and kinetics of phenomena occurring during the interaction of these bioactive glass microparticles with SBF solution. In particular, the network depolymerization, the release of active ions ( $SiO_4^{4-}$ ,  $Ca^{2+}$ ,  $PO_4^{3-}$ ,  $Cu^{2+}$ ) and the formation of surface apatite nanocrystals layer are impacted. Interestingly, copper release demonstrates a strong correlation between the percentage of initial copper doping and the amount released. The latter is mainly provided by the copper involved in the silica network and not from metal nanoparticles, most of them remaining in the microspheres after 14 d of interaction. This understanding holds promising implications for potential therapeutic applications, offering possibilities for both short-term and long-term delivery of therapeutic copper, a pivotal element exhibiting antibacterial activity and pro-angiogenic properties. This study showcases the potential of the spray-drying process as a versatile and efficient method for scalable production in bioactive glass particles fabrication. Future directions involve comprehensive cytotoxicity and antibacterial evaluations and the prospect of associating or functionalizing these bioactive glass microspheres with polymers for the fabrication of porous scaffolds lays the groundwork for the design and development of advanced biomaterials with tailored functionalities for bone substitution.

#### Declaration of competing interest

The authors declare that they have no known competing financial interests or personal relationships that could have appeared to influence the work reported in this paper.

## CRediT authorship contribution statement

**Gabriele Vecchio:** Data curation, Formal analysis, Investigation, Methodology, Writing – original draft. **Vincent Darcos:** Funding acquisition, Methodology, Project administration, Writing – original draft, Writing – review & editing. **Sylvain Le Grill:** Investigation, Writing – review & editing. **Fabien Brouillet:** Methodology, Validation, Writing – review & editing. **Yannick Coppel:** Investigation, Methodology, Validation, Writing – original draft. **Mathieu Duttine:** Investigation, Methodology, Writing – original draft. **Alessandro Pugliara:** Investigation, Methodology, Writing – review & editing.

## Acknowledgements

The authors thank the French National Research Agency for funding (ANR-20-CE19-0019), Yannick Thebault (CIRIMAT) for EDX analysis, Vanessa Soldan (Centre de Biologie Intégrative, Toulouse, France) for ultramicrotomy and Claire Fonquernie (Laboratoire Magma et Volcan, Clermont Ferrand, France) for ICP-OES measurements.

## Supplementary materials

Supplementary material associated with this article can be found, in the online version, at doi:10.1016/j.actbio.2024.05.003.

## References

- [1] J.R. Jones, Review of bioactive glass: from Hench to hybrids, *Acta Biomater.* 9 (2013) 4457–4486, doi:10.1016/j.actbio.2012.08.023.
- [2] I. Cacciotti, Bivalent cationic ions doped bioactive glasses: the influence of magnesium, zinc, strontium and copper on the physical and biological properties, *J. Mater. Sci.* 52 (2017) 8812–8831, doi:10.1007/s10853-017-1010-0.
- [3] M. Erol-Taygun, K. Zheng, A.R. Boccaccini, Nanoscale bioactive glasses in medical applications, *Int. J. Appl. Glass Sci.* 4 (2013) 136–148, doi:10.1111/ijag.12029.
- [4] I.D. Xynos, M.V.J. Hukkanen, J.J. Batten, L.D. Buttery, L.L. Hench, J.M. Polak, Bioglass®45S5 stimulates osteoblast turnover and enhances bone formation in vitro: implications and applications for bone tissue engineering, *Calcif. Tissue Int.* 67 (2000) 321–329, doi:10.1007/s002230001134.
- [5] H. Li, J. Chang, Stimulation of proangiogenesis by calcium silicate bioactive ceramic, *Acta Biomater.* 9 (2013) 5379–5389, doi:10.1016/j.actbio.2012.10.019.
- [6] P. Valerio, M.M. Pereira, A.M. Goes, M.F. Leite, Effects of extracellular calcium concentration on the glutamate release by bioactive glass (BG60S) preincubated osteoblasts, *Biomed. Mater.* 4 (2009) 045011, doi:10.1088/1748-6041/4/4/045011.
- [7] L.R. Rivera, A. Cochis, S. Biser, E. Canciani, S. Ferraris, L. Rimondini, A.R. Boccaccini, Antibacterial, pro-angiogenic and pro-osteointegrative zein-bioactive glass/copper based coatings for implantable stainless steel aimed at bone healing, *Bioact. Mater.* 6 (2021) 1479–1490, doi:10.1016/j.bioactmat.2020.11.001.
- [8] P. Lagarrigue, V. Darcos, C. Tenailleau, B. Duployer, A. Dupret-Bories, S. Cazalbou, D. Poquillon, D. Grossin, C. Combes, J. Soulié, Poly(D,L-lactide)-grafted bioactive glass nanoparticles: from nanobricks to freeze-cast scaffolds for bone substitution, *ACS Appl. Nano Mater.* 5 (2022) 5278–5291, doi:10.1021/acsnm.2c00313.
- [9] A. Braem, N.H.N. Kamarudin, N. Bhaskar, Z. Hadzhieva, A. Mele, J. Soulié, D.P. Linklater, L. Bonilla-Gameros, A.R. Boccaccini, I. Roy, C. Drouet, E.P. Ivanova, D. Mantovani, B. Basu, Biomaterial strategies to combat implant infections: new perspectives to old challenges, *Int. Mater. Rev.* (2023) 1–39, doi:10.1080/09506608.2023.2193784.
- [10] S. Kargozar, M. Mozafari, S. Ghodrati, E. Fiume, F. Baino, Copper-containing bioactive glasses and glass-ceramics: from tissue regeneration to cancer therapeutic strategies, *Mater. Sci. Eng. C* 121 (2021) 111741, doi:10.1016/j.msec.2020.111741.
- [11] J.V. Rau, M. Curcio, M.G. Raucci, K. Barbaro, I. Fasolino, R. Teghil, L. Ambrosio, A. De Bonis, A.R. Boccaccini, Cu-releasing bioactive glass coatings and their in vitro properties, *ACS Appl. Mater. Interfaces* 11 (2019) 5812–5820, doi:10.1021/acsmi.8b19082.
- [12] F. Teng, J. Yuan, P. Tian, Q. Zhang, X. Du, C. Li, W. Wang, Study on the ion-exchange copper-loaded antibacterial glasses, *Ceram. Int.* 48 (2022) 32798–32803, doi:10.1016/j.ceramint.2022.07.205.
- [13] H. Türe, Development of copper-doped bioglass/alginate composite membranes: preliminary results on their characterization and antimicrobial properties, *Mater. Today Commun.* 21 (2019) 100583, doi:10.1016/j.mtcomm.2019.100583.
- [14] S.-J. Bang, S.-K. Jun, Y.-J. Kim, J.-Y. Ahn, H.T. Vu, N. Mandakhbayar, M.-R. Han, J.-H. Lee, J.-B. Kim, J.-S. Kim, J.C. Knowles, H.-S. Kim, H.-H. Lee, J.-S. Shin, J.-H. Lee, Characterization of physical and biological properties of a caries-arresting liquid containing copper doped bioglass nanoparticles, *Pharmaceutics* 14 (2022) 1137, doi:10.3390/pharmaceutics14061137.
- [15] A. Jacobs, G. Renaudin, C. Forestier, J.-M. Nedelec, S. Descamps, Biological properties of copper-doped biomaterials for orthopedic applications: a review of antibacterial, angiogenic and osteogenic aspects, *Acta Biomater.* 117 (2020) 21–39, doi:10.1016/j.actbio.2020.09.044.
- [16] M. Hans, S. Mathews, F. Mücklich, M. Solioz, Physicochemical properties of copper important for its antibacterial activity and development of a unified model, *Biointerphases* 11 (2015) 018902, doi:10.1116/1.4935853.
- [17] R. Nandakumar, C.E. Santo, N. Madayiputhiya, G. Grass, Quantitative proteomic profiling of the Escherichia coli response to metallic copper surfaces, *BioMetals* 24 (2011) 429–444, doi:10.1007/s10534-011-9434-5.
- [18] A.G. Dalecki, C.L. Crawford, F. Wolschendorf, Copper and antibiotics, in: *Adv. Microb. Physiol.*, Elsevier, 2017, pp. 193–260, doi:10.1016/bs.ampbs.2017.01.007.
- [19] G. Borkow, J. Gabbay, Copper as a biocidal tool, *Curr. Med. Chem.* 12 (2005) 2163–2175.
- [20] T. Velnar, T. Bailey, V. Smrkolj, The wound healing process: an overview of the cellular and molecular mechanisms, *J. Int. Med. Res.* 37 (2009) 1528–1542, doi:10.1177/147323000903700531.
- [21] S.R.B. Devi, A. Dhivya, M. K.N. Sulochana, Copper transporters and chaperones: their function on angiogenesis and cellular signalling, *J. Biosci.* 41 (2016) 487–496, doi:10.1007/s12038-016-9629-6.
- [22] A.P. Kornblatt, V.G. Nicoletti, A. Travaglia, The neglected role of copper ions in wound healing, *J. Inorg. Biochem.* 161 (2016) 1–8, doi:10.1016/j.jinorgbio.2016.02.012.
- [23] Bone & Joint Research Group, Centre for human development, stem cells and regeneration, developmental origins of health and disease, institute of developmental sciences, in: J. Kanczler, R. Oreffo (Eds.), *Osteogenesis and Angiogenesis: The Potential for Engineering Bone*, University of Southampton, Southampton, U.K., 2008, pp. 100–114, doi:10.22203/eCM.v015a08. Eur. Cell. Mater. 15.
- [24] A.P. Ingle, N. Duran, M. Rai, Bioactivity, mechanism of action, and cytotoxicity of copper-based nanoparticles: a review, *Appl. Microbiol. Biotechnol.* 98 (2014) 1001–1009, doi:10.1007/s00253-013-5422-8.
- [25] Y. Yang, K. Zheng, R. Liang, A. Mainka, N. Taccardi, J.A. Roether, R. Detsch, W.H. Goldmann, S. Virtanen, A.R. Boccaccini, Cu-releasing bioactive glass/polycaprolactone coating on Mg with antibacterial and anticorrosive properties for bone tissue engineering, *Biomed. Mater.* 13 (2017) 015001, doi:10.1088/1748-605X/aa87f2.
- [26] L. Gaetke, Copper toxicity, oxidative stress, and antioxidant nutrients, *Toxicology* 189 (2003) 147–163, doi:10.1016/S0300-483X(03)00159-8.
- [27] L. Liverani, A. Liguori, P. Zezza, C. Gualandi, M. Toselli, A.R. Boccaccini, M.L. Focarete, Nanocomposite electrospun fibers of poly(ε-caprolactone)/bioactive glass with shape memory properties, *Bioact. Mater.* 11 (2022) 230–239, doi:10.1016/j.bioactmat.2021.09.020.
- [28] F.M. Najafabadi, S. Karbasi, S.Z. Benisi, S. Shojaei, Physical, mechanical, and biological performance of chitosan-based nanocomposite coating deposited on the polycaprolactone-based 3D printed scaffold: potential application in bone tissue engineering, *Int. J. Biol. Macromol.* 243 (2023) 125218, doi:10.1016/j.ijbiomac.2023.125218.
- [29] K. Zheng, A.R. Boccaccini, Sol-gel processing of bioactive glass nanoparticles: a review, *Adv. Colloid Interface Sci.* 249 (2017) 363–373, doi:10.1016/j.cis.2017.03.008.
- [30] C.J. Shih, H.T. Chen, L.F. Huang, P.S. Lu, H.F. Chang, I.L. Chang, Synthesis and in vitro bioactivity of mesoporous bioactive glass scaffolds, *Mater. Sci. Eng. C* 30 (2010) 657–663, doi:10.1016/j.msec.2010.02.006.
- [31] A. Dehghanghadikolaei, J. Ansary, R. Ghoreishi, 1 Mechanical, Manufacturing and Industrial Engineering Department, Oregon State University, Corvallis, Oregon 97331, USA, 2 Mechanical, Manufacturing and Industrial Engineering Department, The University of Toledo, Toledo, OH 43606, USA, 3 Mechanical Engineering Department, Semnan University, Semnan, Iran, Sol-gel process applications: a mini-review, *Proc. Nat. Res. Soc.* 2 (2018) 02008, doi:10.11605/j.pnrs.201802008.
- [32] J. Bejarano, P. Caviedes, H. Palza, Sol-gel synthesis and in vitro bioactivity of copper and zinc-doped silicate bioactive glasses and glass-ceramics, *Biomed. Mater.* 10 (2015) 025001, doi:10.1088/1748-6041/10/2/025001.
- [33] K.C.-W. Wu, Y. Yamauchi, Controlling physical features of mesoporous silicnanoparticles (MSNs) for emerging applications, *J. Mater. Chem.* 22 (2012) 1251–1256, doi:10.1039/C1JM13811A.
- [34] Y. Yamauchi, P. Gupta, K. Sato, N. Fukata, S. Todoroki, S. Inoue, S. Kishimoto, Industrial mass-production of mesoporous silica spherical particles by a spray-drying process: investigation of synthetic conditions, *J. Ceram. Soc. Jpn.* 117 (2009) 198–202, doi:10.2109/jcersj2.117.198.
- [35] L. Ruffel, J. Soulié, Y. Coppel, P. Roblin, F. Brouillet, C. Frances, M. Tourbin, Ibuprofen loading into mesoporous silica nanoparticles using Co-Spray drying: a multi-scale study, *Microporous Mesoporous Mater.* 291 (2020) 109689, doi:10.1016/j.micromeso.2019.109689.
- [36] E. Cianflone, F. Brouillet, D. Grossin, J. Soulié, C. Josse, S. Vig, M.H. Fernandes, C. Tenailleau, B. Duployer, C. Thouron, C. Drouet, Toward smart biomimetic apatite-based bone scaffolds with spatially controlled ion substitutions, *Nanomaterials* 13 (2023) 519, doi:10.3390/nano13030519.
- [37] D.-L. Yang, R.-K. Liu, Y. Wei, Q. Sun, J.-X. Wang, Micro-sized nanoaggregates: spray-drying-assisted fabrication and applications, *Particuology* 85 (2024) 22–48, doi:10.1016/j.partic.2023.03.013.



- [38] M. Faustini, C. Boissière, L. Nicole, D. Grosso, From chemical solutions to inorganic nanostructured materials: a journey into evaporation-driven processes, *Chem. Mater.* 26 (2014) 709–723, doi:[10.1021/cm402132y](https://doi.org/10.1021/cm402132y).
- [39] C. Arpagaus, A. Collenberg, D. Rütli, E. Assadpour, S.M. Jafari, Nano spray drying for encapsulation of pharmaceuticals, *Int. J. Pharm.* 546 (2018) 194–214, doi:[10.1016/j.ijpharm.2018.05.037](https://doi.org/10.1016/j.ijpharm.2018.05.037).
- [40] L. Pontiroli, M. Dadkhah, G. Novajra, I. Tcacencu, S. Fiorilli, C. Vitale-Brovarene, An aerosol-spray-assisted approach to produce mesoporous bioactive glass microspheres under mild acidic aqueous conditions, *Mater. Lett.* 190 (2017) 111–114, doi:[10.1016/j.matlet.2016.12.125](https://doi.org/10.1016/j.matlet.2016.12.125).
- [41] C. Boissière, D. Grosso, A. Chaumonnot, L. Nicole, C. Sanchez, Aerosol route to functional nanostructured inorganic and hybrid porous materials, *Adv. Mater.* 23 (2011) 599–623, doi:[10.1002/adma.201001410](https://doi.org/10.1002/adma.201001410).
- [42] E.M. Littringer, S. Zellnitz, K. Hammernik, V. Adamer, H. Friedl, N.A. Urbanetz, Spray drying of aqueous salbutamol sulfate solutions using the nano spray dryer B-90—the impact of process parameters on particle size, *Dry. Technol.* 31 (2013) 1346–1353, doi:[10.1080/07373937.2013.793701](https://doi.org/10.1080/07373937.2013.793701).
- [43] I.V. Melnyk, Y.L. Zub, E. Véron, D. Massiot, T. Cacciaguerra, B. Alonso, Spray-dried mesoporous silica microspheres with adjustable textures and pore surfaces homogeneously covered by accessible thiol functions, *J. Mater. Chem.* 18 (2008) 1368, doi:[10.1039/b717133a](https://doi.org/10.1039/b717133a).
- [44] N. Baccile, D. Grosso, C. Sanchez, Aerosol generated mesoporous silica particles, *J. Mater. Chem.* 13 (2003) 3011, doi:[10.1039/b307757h](https://doi.org/10.1039/b307757h).
- [45] M. Ide, E. Wallaert, I. Van Driessche, F. Lynen, P. Sandra, P. Van Der Voort, Spherical mesoporous silica particles by spray drying: doubling the retention factor of HPLC columns, *Microporous Mesoporous Mater.* 142 (2011) 282–291, doi:[10.1016/j.micromeso.2010.12.013](https://doi.org/10.1016/j.micromeso.2010.12.013).
- [46] R.C. Suryaprakash, F.P. Lohmann, M. Wagner, B. Abel, A. Varga, Spray drying as a novel and scalable fabrication method for nanostructured  $\text{CsH}_2\text{PO}_4$ , Pt-thin-film composite electrodes for solid acid fuel cells, *RSC Adv.* 4 (2014) 60429–60436, doi:[10.1039/C4RA10259B](https://doi.org/10.1039/C4RA10259B).
- [47] A.B.D. Nandiyanto, K. Okuyama, Progress in developing spray-drying methods for the production of controlled morphology particles: from the nanometer to submicrometer size ranges, *Adv. Powder Technol.* 22 (2011) 1–19, doi:[10.1016/j.apt.2010.09.011](https://doi.org/10.1016/j.apt.2010.09.011).
- [48] X. Yan, C. Yu, X. Zhou, J. Tang, D. Zhao, Highly ordered mesoporous bioactive glasses with superior in vitro bone-forming bioactivities, *Angew. Chem. Int. Ed.* 43 (2004) 5980–5984, doi:[10.1002/anie.200460598](https://doi.org/10.1002/anie.200460598).
- [49] Y.-J. Chou, C.-W. Hsiao, N.-T. Tsou, M.-H. Wu, S.-J. Shih, Preparation and in vitro bioactivity of micron-sized bioactive glass particles using spray drying method, *Appl. Sci.* 9 (2018) 19, doi:[10.3390/app9010019](https://doi.org/10.3390/app9010019).
- [50] H.S. Ningsih, Y.-C. Liu, J.-W. Chen, Y.-J. Chou, Effects of strontium dopants on the in vitro bioactivity and cytotoxicity of strontium-doped spray-dried bioactive glass microspheres, *J. Non-Cryst. Solids* 576 (2022) 121284, doi:[10.1016/j.jnoncrysol.2021.121284](https://doi.org/10.1016/j.jnoncrysol.2021.121284).
- [51] T. Kokubo, H. Takadama, How useful is SBF in predicting in vivo bone bioactivity? *Biomaterials* 27 (2006) 2907–2915, doi:[10.1016/j.biomaterials.2006.01.017](https://doi.org/10.1016/j.biomaterials.2006.01.017).
- [52] W. Stöber, A. Fink, E. Bohn, Controlled growth of monodisperse silica spheres in the micron size range, *J. Colloid Interface Sci.* 26 (1968) 62–69, doi:[10.1016/0021-9797\(68\)90272-5](https://doi.org/10.1016/0021-9797(68)90272-5).
- [53] S.L. Greasley, S.J. Page, S. Sirovica, S. Chen, R.A. Martin, A. Riveiro, J.V. Hanna, A.E. Porter, J.R. Jones, Controlling particle size in the Stöber process and incorporation of calcium, *J. Colloid Interface Sci.* 469 (2016) 213–223, doi:[10.1016/j.jcis.2016.01.065](https://doi.org/10.1016/j.jcis.2016.01.065).
- [54] D.E. Walton, C.J. Mumford, The morphology of spray-dried particles, *Chem. Eng. Res. Des.* 77 (1999) 442–460, doi:[10.1205/026387699526296](https://doi.org/10.1205/026387699526296).
- [55] B. Alonso, A. Douy, E. Véron, J. Perez, M.-N. Rager, D. Massiot, Morphological and textural control of spray-dried mesoporous silica-based spheres, *J. Mater. Chem.* 14 (2004) 2006–2016, doi:[10.1039/B403201B](https://doi.org/10.1039/B403201B).
- [56] E. Boel, R. Koekoek, S. Dedroog, I. Babkin, M.R. Vetrano, C. Clasen, G. Van Den Mooter, Unraveling particle formation: from single droplet drying to spray drying and electrospraying, *Pharmaceutics* 12 (2020) 625, doi:[10.3390/pharmaceutics12070625](https://doi.org/10.3390/pharmaceutics12070625).
- [57] K.M.Z. Hossain, U. Patel, I. Ahmed, Development of microspheres for biomedical applications: a review, *Prog. Biomater.* 4 (2015) 1–19, doi:[10.1007/s40204-014-0033-8](https://doi.org/10.1007/s40204-014-0033-8).
- [58] O.M.V.M. Bueno, C.L. Herrera, C.A. Bertran, M.A. San-Miguel, J.H. Lopes, An experimental and theoretical approach on stability towards hydrolysis of triethyl phosphate and its effects on the microstructure of sol-gel-derived bioactive silicate glass, *Mater. Sci. Eng. C* 120 (2021) 111759, doi:[10.1016/j.msec.2020.111759](https://doi.org/10.1016/j.msec.2020.111759).
- [59] R. Sierra-Ávila, M. Pérez-Alvarez, G. Cadenas-Pliego, C.A. Ávila-Orra, R. Betancourt-Galindo, E. Jiménez-Regalado, R.M. Jiménez-Barrera, J.G. Martínez-Colunga, Synthesis of copper nanoparticles coated with nitrogen ligands, *J. Nanomater.* 2014 (2014) 1–8, doi:[10.1155/2014/361791](https://doi.org/10.1155/2014/361791).
- [60] J.I. Langford, A.J.C. Wilson, Scherrer after sixty years: a survey and some new results in the determination of crystallite size, *J. Appl. Crystallogr.* 11 (1978) 102–113, doi:[10.1107/S0021889878012844](https://doi.org/10.1107/S0021889878012844).
- [61] K. Onoe, Y. Uemura, A. Takeshita, Persistent free radicals (PFRs) formed in pyrolyzed synthetic CHO-type polymers: novel raw material for pfr and better understanding for its formation, *J. Chem. Eng. Jpn.* 56 (2023) 2239287, doi:[10.1080/00219592.2023.2239287](https://doi.org/10.1080/00219592.2023.2239287).
- [62] J. Michalik, D. Brown, J.-S. Yu, M. Danilczuk, J.Y. Kim, L. Kevan, Conduction electron paramagnetic resonance of metal nanoparticles in AIMCM-41 aluminosilica mesoporous molecular sieves, *Phys. Chem. Chem. Phys.* 3 (2001) 1705–1708, doi:[10.1039/B008245G](https://doi.org/10.1039/B008245G).
- [63] D.L. Griscorn, Electron spin resonance in glasses, *J. Non-Cryst. Solids* 40 (1980) 211–272, doi:[10.1016/0022-3093\(80\)90105-2](https://doi.org/10.1016/0022-3093(80)90105-2).
- [64] R.P.S. Chakradhar, B. Yasoda, J.L. Rao, N.O. Gopal, Mixed alkali effect in  $\text{Li}_2\text{O}-\text{Na}_2\text{O}-\text{B}_2\text{O}_3$  glasses containing CuO – an EPR and optical study, *J. Non-Cryst. Solids* 352 (2006) 3864–3871, doi:[10.1016/j.jnoncrysol.2006.06.033](https://doi.org/10.1016/j.jnoncrysol.2006.06.033).
- [65] P. Pascuta, R. Stefan, L.E. Olar, L.C. Bolundut, E. Culea, Effects of copper metallic nanoparticles on structural and optical properties of antimony phosphate glasses co-doped with samarium ions, *Materials* 13 (2020) 5040, doi:[10.3390/ma13215040](https://doi.org/10.3390/ma13215040).
- [66] M. Edén, Structure and formation of amorphous calcium phosphate and its role as surface layer of nanocrystalline apatite: implications for bone mineralization, *Materialia* 17 (2021) 101107, doi:[10.1016/j.mtl.2021.101107](https://doi.org/10.1016/j.mtl.2021.101107).
- [67] E. Leonova, I. Izquierdo-Barba, D. Arcos, L. López-Noriega, N. Hedin, M. Vallet-Regí, M. Edén, Multinuclear solid-state NMR studies of ordered mesoporous bioactive glasses, *J. Phys. Chem. C* 112 (2008) 5552–5562, doi:[10.1021/jp7107973](https://doi.org/10.1021/jp7107973).
- [68] B. Zagajczuk, M. Dziadek, Z. Olejniczak, K. Cholewa-Kowalska, M. Laczka, Structural and chemical investigation of the gel-derived bioactive materials from the  $\text{SiO}_2$ -CaO and  $\text{SiO}_2$ -CaO- $\text{P}_2\text{O}_5$  systems, *Ceram. Int.* 43 (2017) 12742–12754, doi:[10.1016/j.ceramint.2017.06.160](https://doi.org/10.1016/j.ceramint.2017.06.160).
- [69] S. Lin, C. Ionescu, K.J. Pike, M.E. Smith, J.R. Jones, Nanostructure evolution and calcium distribution in sol-gel derived bioactive glass, *J. Mater. Chem.* 19 (2009) 1276, doi:[10.1039/b814292k](https://doi.org/10.1039/b814292k).
- [70] A. Hoppe, R. Meszaros, C. Stähli, S. Romeis, J. Schmidt, W. Peukert, B. Marelli, S.N. Nazhat, L. Wondraczek, J. Lao, E. Jallot, A.R. Boccaccini, In vitro reactivity of Cu doped 45S5 Bioglass® derived scaffolds for bone tissue engineering, *J. Mater. Chem. B* 1 (2013) 5659, doi:[10.1039/c3tb21007c](https://doi.org/10.1039/c3tb21007c).
- [71] M. Soorani, E. Mele, J.K. Christie, Structural effects of incorporating  $\text{Cu}^+$  and  $\text{Cu}^{2+}$  ions into silicate bioactive glasses using molecular dynamics simulations, *Mater. Adv.* (2023), doi:[10.1039/D2MA00872F](https://doi.org/10.1039/D2MA00872F).
- [72] P.N. Gunawidjaja, R. Mathew, A.Y.H. Lo, I. Izquierdo-Barba, A. García, D. Arcos, M. Vallet-Regí, M. Edén, Local structures of mesoporous bioactive glasses and their surface alterations *in vitro*: inferences from solid-state nuclear magnetic resonance, *Philos. Trans. R. Soc. Math. Phys. Eng. Sci.* 370 (2012) 1376–1399, doi:[10.1098/rsta.2011.0257](https://doi.org/10.1098/rsta.2011.0257).
- [73] N. Gupta, D. Santhiya, S. Murugavel, A. Kumar, A. Aditya, M. Ganguli, S. Gupta, Effects of transition metal ion dopants (Ag, Cu and Fe) on the structural, mechanical and antibacterial properties of bioactive glass, *Colloids Surf. Physicochem. Eng. Asp.* 538 (2018) 393–403, doi:[10.1016/j.colsurfa.2017.11.023](https://doi.org/10.1016/j.colsurfa.2017.11.023).
- [74] Y. Sun, Z. Zhang, L. Liu, X. Wang, FTIR, Raman and NMR investigation of CaO- $\text{SiO}_2$ - $\text{P}_2\text{O}_5$  and CaO- $\text{SiO}_2$ - $\text{TiO}_2$ - $\text{P}_2\text{O}_5$  glasses, *J. Non-Cryst. Solids* 420 (2015) 26–33, doi:[10.1016/j.jnoncrysol.2015.04.017](https://doi.org/10.1016/j.jnoncrysol.2015.04.017).
- [75] R.J. Kirkpatrick, R.K. Brow, Nuclear magnetic resonance investigation of the structures of phosphate and phosphate-containing glasses: a review, *Solid State Nucl. Magn. Reson.* 5 (1995) 9–21, doi:[10.1016/0926-2040\(95\)00042-0](https://doi.org/10.1016/0926-2040(95)00042-0).
- [76] R.L. Karlinsey, A.C. Mackey, E.R. Walker, K.E. Frederick, Preparation, characterization and in vitro efficacy of an acid-modified  $\beta$ -TCP material for dental hard-tissue remineralization, *Acta Biomater.* 6 (2010) 969–978, doi:[10.1016/j.actbio.2009.08.034](https://doi.org/10.1016/j.actbio.2009.08.034).
- [77] Y. Coppel, Y. Prigent, G. Grégoire, Characterization of hydrogenated dentin components by advanced  $^1\text{H}$  solid-state NMR experiments, *Acta Biomater.* 120 (2021) 156–166, doi:[10.1016/j.actbio.2020.08.022](https://doi.org/10.1016/j.actbio.2020.08.022).
- [78] M. Ben Osman, S. Diallo-García, V. Herledan, D. Broui, T. Yoshioka, J. Kubo, Y. Millot, G. Costentin, Discrimination of surface and bulk structure of crystalline hydroxyapatite nanoparticles by NMR, *J. Phys. Chem. C* 119 (2015) 23008–23020, doi:[10.1021/acs.jpcc.5b08732](https://doi.org/10.1021/acs.jpcc.5b08732).
- [79] E. San Andrés, A. Del Prado, I. Mártel, G. González-Díaz, D. Bravo, F.J. López, M. Fernández, W. Bohne, J. Röhrich, B. Selle, I. Sieber, Bonding configuration and density of defects of  $\text{SiO}[\text{sub } x\text{H}][\text{sub } y]$  thin films deposited by the electron cyclotron resonance plasma method, *J. Appl. Phys.* 94 (2003) 7462, doi:[10.1063/1.1626798](https://doi.org/10.1063/1.1626798).
- [80] I.A. Rahman, P. Vejayakumaran, C.S. Sipaut, J. Ismail, C.K. Chee, Size-dependent physicochemical and optical properties of silica nanoparticles, *Mater. Chem. Phys.* 114 (2009) 328–332, doi:[10.1016/j.matchemphys.2008.09.068](https://doi.org/10.1016/j.matchemphys.2008.09.068).
- [81] S. Rovani, J. Santos, P. Corio, D. Fungaro, An alternative and simple method for the preparation of bare silica nanoparticles using sugarcane waste ash, an abundant and despised residue in the Brazilian industry, *J. Braz. Chem. Soc.* (2019), doi:[10.21577/0103-5053.20190049](https://doi.org/10.21577/0103-5053.20190049).
- [82] S. Akhtach, Z. Tabia, K. El Mabrouk, M. Bricha, R. Belkhou, A comprehensive study on copper incorporated bio-glass matrix for its potential antimicrobial applications, *Ceram. Int.* 47 (2021) 424–433, doi:[10.1016/j.ceramint.2020.08.149](https://doi.org/10.1016/j.ceramint.2020.08.149).
- [83] N. Vandecandelaere, C. Rey, C. Drouet, Biomimetic apatite-based biomaterials: on the critical impact of synthesis and post-synthesis parameters, *J. Mater. Sci. Mater. Med.* 23 (2012) 2593–2606, doi:[10.1007/s10856-012-4719-y](https://doi.org/10.1007/s10856-012-4719-y).
- [84] F. Errassifi, S. Sarda, A. Barroug, A. Legroui, H. Sfhi, C. Rey, Infrared, Raman and NMR investigations of risedronate adsorption on nanocrystalline apatites, *J. Colloid Interface Sci.* 420 (2014) 101–111, doi:[10.1016/j.jcis.2014.01.017](https://doi.org/10.1016/j.jcis.2014.01.017).
- [85] N.M. Alves, I.B. Leonor, H.S. Azevedo, R.L. Reis, J.F. Mano, Designing biomaterials based on biomineralization of bone, *J. Mater. Chem.* 20 (2010) 2911, doi:[10.1039/b910960a](https://doi.org/10.1039/b910960a).
- [86] C. Turdean-Ionescu, B. Svensson, J. Grins, I. Izquierdo-Barba, A. García, D. Arcos, M. Vallet-Regí, M. Edén, Composition-dependent in vitro apatite formation at mesoporous bioactive glass-surfaces quantified by solid-state NMR and powder XRD, *RSC Adv.* 5 (2015) 86061–86071, doi:[10.1039/C5RA13410B](https://doi.org/10.1039/C5RA13410B).



- [87] P.N. Gunawidjaja, I. Izquierdo-Barba, R. Mathew, K. Jansson, A. García, J. Grins, D. Arcos, M. Vallet-Regí, M. Edén, Quantifying apatite formation and cation leaching from mesoporous bioactive glasses in vitro: a SEM, solid-state NMR and powder XRD study, *J. Mater. Chem.* 22 (2012) 7214, doi:[10.1039/c2jm15066b](https://doi.org/10.1039/c2jm15066b).
- [88] W. Kolodziejski, J. Klinowski, Kinetics of cross-polarization in solid-state NMR: a guide for chemists, *Chem. Rev.* 102 (2002) 613–628, doi:[10.1021/cr000060n](https://doi.org/10.1021/cr000060n).
- [89] Y. Yu, H. Guo, M. Pujari-Palmer, B. Stevansson, J. Grins, H. Engqvist, M. Edén, Advanced solid-state  $^1\text{H}/^{31}\text{P}$  NMR characterization of pyrophosphate-doped calcium phosphate cements for biomedical applications: the structural role of pyrophosphate, *Ceram. Int.* 45 (2019) 20642–20655, doi:[10.1016/j.ceramint.2019.07.047](https://doi.org/10.1016/j.ceramint.2019.07.047).
- [90] M.C. Chang, J. Tanaka, FT-IR study for hydroxyapatite/collagen nanocomposite cross-linked by glutaraldehyde, *Biomaterials* 23 (2002) 4811–4818, doi:[10.1016/S0142-9612\(02\)00232-6](https://doi.org/10.1016/S0142-9612(02)00232-6).
- [91] S. Chitra, P. Bargavi, M. Balasubramaniam, R.R. Chandran, S. Balakumar, Impact of copper on in-vitro biomineralization, drug release efficacy and antimicrobial properties of bioactive glasses, *Mater. Sci. Eng. C* 109 (2020) 110598, doi:[10.1016/j.msec.2019.110598](https://doi.org/10.1016/j.msec.2019.110598).
- [92] M. Mozafari, F. Moztarzadeh, M. Tahriri, Investigation of the physico-chemical reactivity of a mesoporous bioactive  $\text{SiO}_2\text{--CaO--P}_2\text{O}_5$  glass in simulated body fluid, *J. Non-Cryst. Solids* 356 (2010) 1470–1478, doi:[10.1016/j.jnoncrsol.2010.04.040](https://doi.org/10.1016/j.jnoncrsol.2010.04.040).
- [93] M. Mami, A. Lucas-Girot, H. Oudadesse, R. Dorbez-Sridi, F. Mezahi, E. Dietrich, Investigation of the surface reactivity of a sol-gel derived glass in the ternary system  $\text{SiO}_2\text{--CaO--P}_2\text{O}_5$ , *Appl. Surf. Sci.* 254 (2008) 7386–7393, doi:[10.1016/j.apsusc.2008.05.340](https://doi.org/10.1016/j.apsusc.2008.05.340).
- [94] C.G. Pantano, A.E. Clark, L.L. Hench, Multilayer corrosion films on bioglass surfaces, *J. Am. Ceram. Soc.* 57 (1974) 412–413, doi:[10.1111/j.1151-2916.1974.tb11429.x](https://doi.org/10.1111/j.1151-2916.1974.tb11429.x).
- [95] M.R. Filgueiras, G. La Torre, L.L. Hench, Solution effects on the surface reactions of a bioactive glass, *J. Biomed. Mater. Res.* 27 (1993) 445–453, doi:[10.1002/jbm.820270405](https://doi.org/10.1002/jbm.820270405).
- [96] L.L. Hench, J.M. Polak, Third-generation biomedical materials, *Science* 295 (2002) 1014–1017, doi:[10.1126/science.1067404](https://doi.org/10.1126/science.1067404).